Influence of grain growth on the thermal structure of inner protoplanetary discs

Sofia Savvidou

Lund Observatory
Lund University

Abstract

Protoplanetary discs surround young stars for the first few million years after their formation and they are the birthplaces of planetary systems. The thermal structure of the discs is regulated by their dust content and the opacity that it provides. The aim of this project is to investigate the effect grain growth has on the structure of the protoplanetary discs.

Hydrodynamical simulations have been coupled to a new opacity model, which can calculate the opacity as a function of temperature for a dust population taking into account the particle size, composition and abundance. Single-size simulations are investigated for different turbulent strengths. Full size distributions are also explored that take into account coagulation and fragmentation of dust particles. For the single size simulations it was found that discs with small grains, from 0.1 to 10 μm have similar thermal structures at high turbulence. There exists a slight progressive drop with increasing orbital distance in the temperature or aspect ratio of these discs for the specified grain sizes. On the other hand, discs with grains of 1 mm are around 50% colder at midplane within the first few AU, compared to discs with small grains, but this difference is diminished after approximately 10 AU. The 0.1 mm grains lead to discs that remain 60% hotter even at the outer boundaries of the discs. The location of the iceline depends on the particle size, as it moves inwards as the particles size increases and it is inside 1 AU for the larger particles. In general, decreasing turbulence leads to colder discs and shrinks even further the differences between various grain sizes. The iceline in this case typically moves inside 1 AU even for smaller grain sizes.

Two different full grain size distributions were modelled. In the first, the number density follows a power-law inspired by a coagulation/fragmentation equilibrium (Dohnanyi, 1969; Tanaka et al., 1996). The second begins with the same mass distribution, but takes into consideration the relative velocities for particles of different sizes and divides particles into regimes with different slopes for the mass distribution depending on their sizes and therefore aerodynamical properties (Birnstiel et al., 2011). Both models converge near the outer boundaries of the discs simulated here and they show a strong influence from the particles of around 0.1 mm in size. The inner parts of the disc simulated here, show a difference because of the upper boundary of each size distribution. In the more complex model the upper boundary is determined by the fragmentation barrier which leaves only smaller particles in the inner disc. On the contrary, the simple model following the Dohnanyi (1969) distribution has an arbitrarily fixed upper boundary which means that larger particles are present in this case. These have lower opacities and therefore enhance the cooling rate and decrease the disc's temperature and aspect ratio. The iceline in both of the grain size distribution models is around 3 AU.

The grain sizes distribution simulations show that in discs with significant viscous heating, often-used opacity models based on μm-sized dust grains only are not a good approximation in order to create more realistic theoretical models.

Populärvetenskaplig beskrivning

Intresset för att studera protoplanetära diskar har ökat inom forskarvärlden i och med de observationer av dem som har gjorts de senaste åren. Observatoriet Atacama Large Millimeter Array (ALMA) i Chile har observerat flertalet protoplanetära diskar i enastående detalj. Dessa observationer har motiverat forskare till ytterligare teoretiska studier av protoplanetära diskar och deras dynamiska utveckling. Syftet bakom detta projekt är att skapa en mer realistisk modell för strukturen av protoplanetär diskar. Typiskt för äldre teoretiska modeller är att enbart en stoftstorlek och dess motsvarande opacitet inkluderas, men, observationer indikerar att stoftkornen växer och driver i den protoplanetära disken. Med det i åtanke, har en mer realistisk modell för distributionen av stoftstorlekar använts i detta projekt.

I detta projektet utför jag hydrodynamiska simuleringar som initialt använder enbart en stoftstorlek och motsvarande medelvärden för opaciteten, som i sin tur är beroende på temperaturen. Detta tillåter oss att jämföra de strukturer som bildas, som en funktion av stoftstorleken. Dessa resultat ger då en första indikation påhur de olika stoftstorlekarna påverkar disk strukturen. Nästa steg är att skapa en distribution av stoftstorlekar och undersöka dess effekter påvärmestrukturen i disken. Vi finner att denna diskstruktur påverkas av att stoftet växer, och modeller som enbart inkluderar en stoftstorlek inte kan beskriva strukturerna väl. Dessa fynd är viktiga för att många av processerna bakom planetbildning (småstenar som driver i disken, planetesimalbildning, anhopningen av småstenar, samt planet migration) påverkas direkt av diskens temperatur.

Contents

List of Figures

Chapter 1

Introduction

1.1 What is a protoplanetary disc?

The nebula hypothesis, a theory about the formation of the Solar System, was proposed by Swedenborg (1734), further developed and published by Immanuel Kant in 1755 and independently analysed and published by Pierre Simon de Laplace in 1796 (discussion in Woolfson, 1993). According to this theory and our current knowledge, planet formation is entwined with the formation of a protostar inside the "stellar nurseries" of molecular clouds. These "stellar nurseries" are fractions of dense, cool gas and dust that undergo gravitational collapse when their self-gravity exceeds thermal, turbulent and magnetic support (Larson, 1969; Penston, 1969; Hunter, 1977; Shu, 1977; Larson, 2003, for review). During this collapse, that has a duration of $10^5 - 10^6$ yr, material falls towards the center of the core, forming the protostar. Most of the cloud cores that form stars have been observed to be rotating (Goodman et al., 1993), but the magnitude of the angular momentum is not possible to be contained in the protostar alone, even if we consider that magnetic fields carry some angular momentum away. Matter with high specific angular momentum cannot fall towards the protostar, but it rather orbits around it, until a centrifugally supported disc forms with an equatorial plane approximately perpendicular to the rotation axis of the collapsing core. Energy from the gravitational collapse is converted to orbital kinetic energy and heat. Typical temperature values for the disc are ~1500 K at 1 AU, as material there falls deep in the potential well of the system and ~100 K at 10 AU (Larson, 1969). The accretion to the star continues through this disc, but in order for matter to be transported inwards, angular momentum has to be transported outwards through the disc (Lynden-Bell & Pringle, 1974). These discs surround the young stars at their first few million years and since planet formation is expected to take place there, they are called protoplanetary discs.

Recently, the Atacama Large Millimeter/submillimeter Array (ALMA) observatory in Chile has observed several protoplanetary discs (Figure 1.1) in unprecedented detail. The description above regarding the formation of a protoplanetary disc around a young star has been recently supported by the ALMA observations of two protostellar systems, in

(a) HL Tau, ALMA Partnership et al. (2015)   *(b) AS 209, Fedele et al. (2018)*   *(c) TW Hydrae, Andrews et al. (2016)*
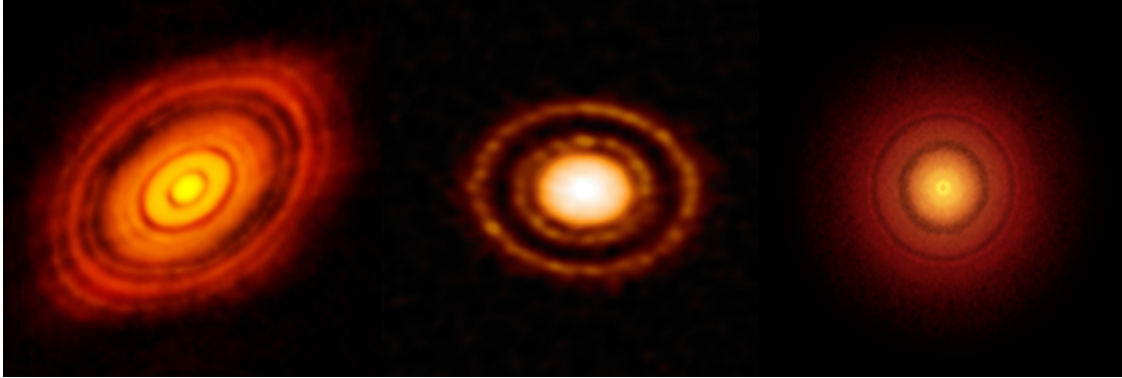
Figure 1.1: Protoplanetary disc images from ALMA

the L1630 cloud of Orion at a distance of 400 pc, HH 111 and HH212, which are approximately 40000 yr old (Lee et al., 2018). Such observations will provide more information and parameters to be considered for accurate models. In Figure 1.1a we can see the protoplanetary disc around HL Tauri or HL Tau, located at a distance of approximately 140 pc from the Earth, in the Taurus Molecular Cloud, the closest large star forming region. The system is very young, estimated to be less than 1 Myr old. TW Hydrae is a relatively old system, approximately 10 Myr, close to Earth at 54 ± 6 pc. The AS 209 system is located in the Ophiuchus star forming region, 126 pc away and is estimated to be 0.5-1 Myr. All of these observations are of the dust continuum emission at around 1 mm. The gaps that can be seen in all of the systems have been attributed to giant planet formation (Dipierro et al., 2015; Kanagawa et al., 2015; Akiyama et al., 2016; Fedele et al., 2018) or turbulence by magnetorotational instability (Balbus & Hawley, 1991). They can also be an effect of icelines, the location in a disc where water-ice sublimates, while recent research has indicated that multiple icelines, such as H_2O, CO_2 or NH_3 can be responsible for the gaps (Okuzumi et al., 2012; Zhang et al., 2015; Pinilla et al., 2017). In general, observational data can constrain several parameters related to the disc structure, but they cannot provide all the necessary information to understand protoplanetary discs in depth.

1.2   Motivation

The disc structure is determined by a feedback loop (Figure 1.2). In particular, the temperature (T) and aspect ratio (H/r) of a protoplanetary disc affect the relative velocities (Δu) for grains of different sizes. These have an effect on the possible grain sizes and their number densities in the disc. The sizes and subsequently their surface densities influence the opacity (κ) of the disc, which affects its cooling rate (D) and hence changes its tem-

perature and aspect ratio and so on, so forth. This feedback loop can be seen in Figure 1.2. Since a distribution of grain sizes and the corresponding opacities affect in many ways the general structure, it is important to include it in disc models and study its effect on the disc.

Even though the goal of theoretical models is to simulate protoplanetary discs as realistically as possible, typically they only include specific parts of the feedback loop. In the following paragraphs, an overview will be given of previous works, dividing each of them into the part of the feedback loop that they belong to. For each group the title lists the physics that is included by giving the appropriate labels of the feedback loop (Figure 1.2).
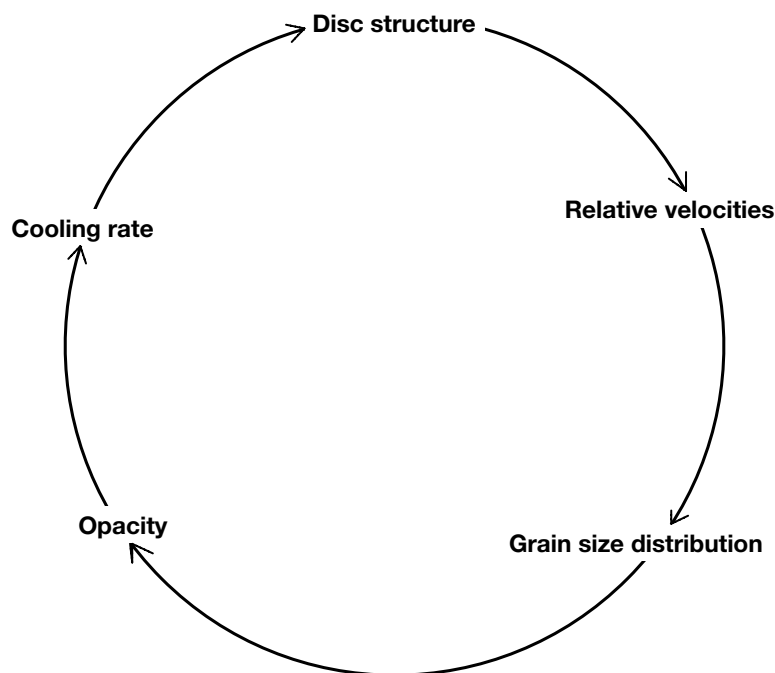
Figure 1.2: Feedback loop

<u>Relative velocities + Grain size distribution</u>

Early on, Safronov (1969) worked on dust growth within the context of planet formation and on the time evolution equation for grain size distributions (often called Smoluchowski equation (Smoluchowski, 1916)). Additionally, a lot of work was done on dust dynamics and how they would affect collisional outcomes and, as a consequence, coagulation and fragmentation of dust particles (Weidenschilling, 1980, 1984; Nakagawa, et al., 1981). A grain size distribution has been widely assumed to follow a power-law derived from the

equilibrium between coagulation and fragmentation, inspired by the work of Dohnanyi (1969) on the number density distribution of objects in the asteroid belt. The number density, thus, can be approximated as $n(s) \propto s^{\xi}$, where s is the grain size and ξ a constant. Several attempts were made in order to define this constant, mainly through analytical calculations combined with observational data (e.g. Mathis et al., 1977), but also through experimental studies (e.g. Davis & Ryan, 1990). It was shown by Tanaka et al. (1996) that the ξ constant is independent of the specific parameters of the collisional outcome model, as long as it is self-similar, which in this case means that the outcome of impacts between dust grains depends on the masses of two colliding particles only through their ratio.

However, such a description of a grain size distribution with only one power law is a simplification, since it only takes into account the coagulation/fragmentation equilibrium. More recently, the work on grain size distributions has been aided by laboratory experiments of dust collisions (review by Blum & Wurm, 2008; Güttler, et al., 2010). Such experiments determine what the collisional outcomes are between different or equal sized particles for different relative velocities. They also help in creating models to simulate such collisions accurately and they can be used in the effort of understanding which processes are relevant within the context of planetesimal formation in protoplanetary discs (e.g. Zsom, et al., 2010). If additional effects are also taken into account, such as cratering or different regimes due to size-dependent relative velocities, then the size distribution is described by broken power laws (Birnstiel et al., 2011). The grain size distribution will be further discussed in Chapters 2.3.1 and 3.2.

To summarize, the studies that were discussed above, focused on the local distribution of grains in a protoplanetary disc patch due to fragmentation and growth by coagulation and typically assume that the gas disc does not evolve in time or reacts to the growth of solids.

Opacity

An important aspect of the structure of a protoplanetary disc is opacity, which is mainly determined by dust and plays an important role in the thermal structure of discs. As a first step, some work has been done on opacity alone within the context of protoplanetary discs (Miyake & Nakagawa, 1993; Draine, 2006; Cuzzi et al., 2014). The goal of those works is to create a simple opacity model that can describe as realistically as possible the dust opacity and can be then used in disc simulations or help in the interpretation of disc observations. Alongside the theoretical models, several observations of the dust emission have been performed in order to connect opacity with the particle sizes present in the protoplanetary discs. (Natta, et al., 2007; Andrews & Williams, 2005, 2007; Rodmann, et al., 2006; Lommen, et al., 2009; Ricci, et al., 2010, 2011; Ubach, et al., 2012).

Disc structure + Grain size distribution

Several works in the recent years have aimed to couple the dust and gas components of

protoplanetary discs in simulations and in most of the cases such models include a grain size distribution. However, the models that will be discussed here simulate the gas component of a protoplanetary disc and how the dust component is affected by the gas, but the solids do not influence the gas. Even without the back-reactions of dust on gas, modelling grain size distributions can be computationally challenging, given the long list of effects and parameters to be taken into account, especially using N-body like techniques to treat dust particles. As a consequence, some of the first attempts on this kind of models were made using the Monte-Carlo method (Ormel, et al., 2007; Ormel & Spaans, 2008) and the goal was to examine how the internal structure of dust affects the collisional evolution of the particles and the disc structure. The Monte-Carlo method has been also used in Zsom, et al. (2010, 2011), while in this work the experimental collisional outcomes from Güttler, et al. (2010) were implemented and the effect of the porosity and settling of the dust grains on the collisional outcomes was tested. More recently, the coagulation/fragmentation equilibrium was included in steady-state simulations (Brauer et al., 2008) and time-dependent disc models that focused on the dust grain porosity and its effect on the dust evolution (Okuzumi et al., 2012). In Birnstiel et al. (2010) a model similar to Brauer et al. (2008) was presented that combined a gas disc evolution code with a dust evolution code aiming at the investigation of how the evolution of the protoplanetary disc affects the growth and transport of dust. In the presented works, the feedback of the dust on the gas disc structure is not taken into account.

Disc structure + Opacity + Cooling rate

The category of models that was described above neglected the effects of opacity, even though the dust opacity regulates the cooling rate of the disc, which affects the disc structure. In recent years, some studies tried to fill this gap by including the effect of dust opacity in disc simulations. Oka et al. (2011) performed 1+1D simulation [1] focusing on the effect that water-ice opacity has to the location of the iceline. In the aforementioned study the wavelength-dependent opacities of water-ice and silicates (see Chapter 2.2) are directly used when calculating the radiative transfer. In Bitsch et al. (2013, 2015a,b) the Bell & Lin opacity profile is followed (in Bitsch et al. (2013) constant opacity discs were also modeled) and 2D simulations are performed using the NIRVANA and the FARGOCA code adding radial heat diffusion. The Bell & Lin (1994) opacity model gives approximate values for the frequency averaged opacities within specific temperature regimes (e.g. ice grains, evaporation of ice grains, metal grains, etc.). The fixed opacity profile then gives the cooling rate and with it the disc structure.

Even though including the opacity feedback in disc simulations is an important improvement, the aforementioned studies did not include the effect of grain growth and fragmentation.

---

[1] In the 1+1D approach, the vertical structure of each annulus is solved independently and then all of the annuli are used to construct the radial and vertical structure of the disc.

Disc structure + Grain size distribution + Opacity

Schmitt, et al. (1997) coupled the dust and gas evolution in 1D simulations, while they also took into consideration the grain opacity. For the mean opacity calculations they followed the approach of Henning & Stognienko (1996), which is similar to the Bell & Lin (1994) opacity model approach. Moreover, the size distribution follows the Mathis et al. (1977) power-law. It was found that since grains determine the opacity, their evolution will subsequently change the opacity and therefore affect the structure and evolution of a protoplanetary disc. Prior to this study, Mizuno, et al. (1988) and Mizuno (1989) included the dust component evolution in accretion discs and used the results to perform grain opacity calculations. In Suttner & Yorke (2001) the coagulation/fragmentation equilibrium is included in order to investigate how the dust emission is affected by the grain size distribution and its corresponding opacity. In this work the size distribution follows the Mathis et al. (1977) power-law and opacity was calculated using Mie theory. In the studies discussed above the back-reaction of the opacity onto the disc structure was not taken into account.

Motivation

In the previous paragraphs some examples were given of the work that has been done in the context of grain growth within protoplanetary discs. Nevertheless, previous models were based on several simplifications, most important of which was that they neglected parts of the feedback loop that defines protoplanetary disc structures (e.g. Birnstiel et al., 2011) or used simplified assumptions for the opacity (e.g. Bitsch et al., 2013). The few attempts that have been made to include the dust feedback on the gas of the disc, were first of all 1D simulations, in contrast to the 2D models that will be presented here. Secondly, the opacity is either not included in the actual simulations or the opacities were included only for single fixed grain sizes. The motivation for this project is to approach a more realistic model for disc structures and their evolution and more specifically to simulate the whole feedback loop including a detailed opacity module. For this reason, I will consider how grain dynamics and grain size distributions affect the opacity and as a consequence the thermal structure of the disc in order to simulate the whole feedback loop. As far as the grain size distribution is concerned, two models were used for the simulations of this thesis. A simple power-law model following Dohnanyi (1969); Tanaka et al. (1996) and also a more complex model following Birnstiel et al. (2011). Moreover, an opacity module was included in 2D hydrodynamical disc simulations in order to more accurately calculate the opacity of the dust grain distribution and account for the back-reactions of dust to gas. In this opacity module, the Rosseland and Planck mean opacities as a function of temperature are used and they are calculated via Mie theory (see Chapters 2.2 and 3.1). The simulations were run until the disc reached thermal equilibrium.

Chapter 2

Theory

2.1 Disc structure & evolution

The structure of a protoplanetary disc is important since it can shed light to several stages of formation and growth of planets, such as growth of dust particles to pebbles, movement of pebbles because of gas drag, formation of planetesimals and planetary cores, as well as planet migration. In order to describe the system's time evolution we utilize the continuity and the Navier-Stokes equations in spherical coordinates.

The vertical structure is defined as the steady-state solutions of the hydrodynamic equation and the Poisson equation for the gravitational potential. We assume that the mass of the disc $M_{disc} \ll M_{\star}$, where $M_{\star}$ is the mass of the protostar and that the scale height $H \ll r$, with r the radius of the disc. Then in order to find the equilibrium we must balance the vertical gravitational acceleration g_z to the acceleration due to the vertical gas pressure gradient $\frac{1}{\rho}\frac{dP}{dz}$, where z is the height of the disc and ρ is the gas density

$$\frac{1}{\rho}\frac{dP}{dz} = -g_z \ . \tag{2.1}$$
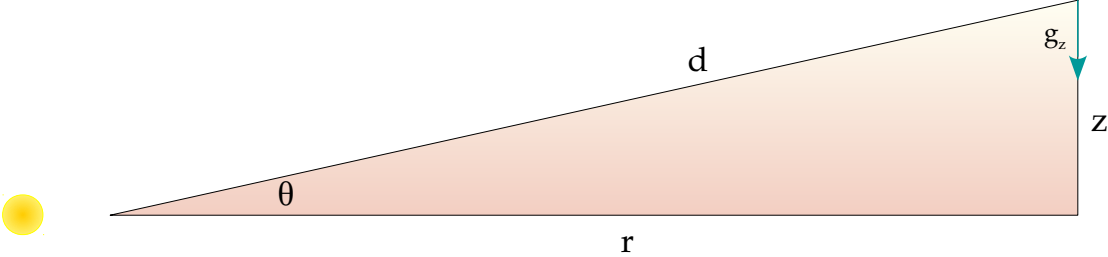
Figure 2.1: Sketch for the calculation of the vertical hydrostatic equilibrium

From the geometry in Figure 2.1 we see that the vertical gravitational acceleration is

$$g_z = F_{g_z} \sin\theta, \tag{2.2}$$

where F_{g_z} is the vertical component of the gravitational force for a parcel of gas at (r,z). Then since $d^2 = r^2 + z^2$

$$g_z = \frac{GM_\star}{d^2}\frac{z}{d} = \frac{GM_\star z}{(r^2 + z^2)^{3/2}} \tag{2.3}$$

We usually assume for discs that $z \ll r$ so that so the expression becomes

$$g_z \simeq \frac{GM_\star z}{r^3} \ . \tag{2.4}$$

Assuming that the disc is vertically isothermal the pressure is

$$P = \rho c_s^2 \ , \tag{2.5}$$

where c_s the sound speed. We then have

$$c_s^2 \frac{d\rho}{dz} = -\frac{GM_\star z \rho}{r^3} \ , \tag{2.6}$$

which has the solution

$$\rho(z) = \rho_0 \exp\left(-\frac{z^2}{2H^2}\right). \tag{2.7}$$

The constant ρ_0 is the midplane density and we can calculate it by solving the surface density integral

$$\Sigma_g = \int_{-\infty}^{+\infty} \rho(z)dz \Rightarrow \tag{2.8}$$

$$\rho_0 = \frac{\Sigma_g}{\sqrt{2\pi}H} \ . \tag{2.9}$$

The vertical pressure scale height H is defined as

$$H = \frac{c_s}{\Omega} \ . \tag{2.10}$$

The sound speed is connected to the temperature T, since by definition $c_s = \sqrt{P/\rho}$ or

$$c_s = \sqrt{\frac{k_B T}{\mu m_p}} \ , \tag{2.11}$$

where k_B is the Boltzmann constant, m_p is the proton mass and μ is the mean molecular weight in units of the proton mass. The Keplerian angular velocity is given by

$$\Omega = \sqrt{\frac{GM_\star}{r^3}} \ . \tag{2.12}$$

If we substitute Equation 2.11 into (2.10) we can find the relationship between temperature T and aspect ratio H/r assuming hydrostatic equilibrium,

$$T = \left(\frac{H}{r}\right)^2 \frac{GM_\star}{r} \frac{\mu m_p}{k_B} \ . \tag{2.13}$$

Another important quantity affecting the structure and evolution of a protoplanetary disc is viscosity. In this project the Shakura-Sunyaev α prescription is followed for the derivation of viscosity

$$\nu = \alpha c_s H \ , \tag{2.14}$$

where α is the Shakura-Sunyaev parameter (Shakura & Sunyaev, 1973), a dimensionless quantity that measures how efficient the angular momentum transport is due to viscosity. The typical range of values for α is 10^{-4} to 10^{-2}. In this context the mass flux through the disc, can be written as

$$\dot{M} = 3\pi\nu\Sigma_g = 3\pi\alpha c_s H\Sigma_g \ . \tag{2.15}$$

We should next consider the energy profile of a protoplanetary disc and its time evolution

$$\frac{\partial E_R}{\partial t} + \nabla \cdot \mathbf{F} = \rho\kappa_P[B(T) - cE_R] \tag{2.16}$$

$$\frac{\partial \epsilon}{\partial t} + \nabla \cdot (\mathbf{u} \cdot \nabla)\epsilon = -P\nabla \cdot \mathbf{u} - \rho\kappa_P[B(T) - cE_R] + Q^+ + S \ . \tag{2.17}$$

The radiative energy density $E_R = \alpha_R T^4$ is independent from the thermal energy density $\epsilon = \rho c_v T$, with c_v the specific heat at constant volume. Also $B(T) = 4\sigma T^4$, where σ is the Stefan-Boltzmann constant and κ_P the Planck mean opacity (introduced in Chapter 2.2). Q^+ is the viscous dissipation or heating function and S is the stellar heating component (Levermore & Pomraning, 1981; Dobbs-Dixon, et al., 2010; Commerçon, et al., 2011). $\mathbf{F}$ is the radiation flux in our simulations, for which the flux-limited diffusion (FLD) is used as described in Levermore & Pomraning (1981)

$$\mathbf{F} = -\frac{\lambda c 4\alpha_R T^3}{\rho(\kappa_R + \sigma)}\nabla T \ . \tag{2.18}$$

In the flux-limited diffusion equation, c is the speed of light, α_R is the radiation constant, κ_R is the Rosseland mean opacity (see Chapter 2.2), σ is the scattering coefficient, in this case set to zero and λ the flux-limiter of Kley (1989). It is assumed that the radiation energy density E_R is lower than the thermal energy density ϵ. We can calculate only the viscous heating by setting the stellar heating component S=0.

The viscous heating component per unit surface area, caused by an effective viscosity induced by the disc's turbulence, is

$$Q^+ = \frac{9}{8}\Sigma\nu\Omega_K^2 \tag{2.19}$$

and if we are considering α-viscosity discs we can also write the expression as

$$Q^+ = \frac{9}{8}\Sigma\alpha c_s^2\Omega_K \ . \tag{2.20}$$

The radiative, blackbody cooling per unit surface area, for a disc without stellar irradiation is

$$Q^- = \frac{2\sigma T^4}{\tau_{eff}} \ , \tag{2.21}$$

with σ the Steffan-Boltzmann constant and $\tau_{eff} = \frac{1}{2}\kappa_R\Sigma$ the effective optical depth (see Equation 2.25). Equating viscous heating (Equation 2.20) and radiative cooling (Equation 2.21) we find that the aspect ratio as a function of radius follows

$$\frac{H}{r} = \left(\frac{9}{32}\frac{k_B^4\Sigma_0^2\alpha}{\mu^4 m_p^4 (GM_\star)^{5/2}}\right)^{1/6}\kappa_R^{1/6}r^{1/4-p/3} \tag{2.22}$$

and it was also assumed that the disc's surface density follows $\Sigma = \Sigma_0 r^{-p}$, with Σ_0 and p constants. Nevertheless, since opacity is a function of temperature, it is also a function of aspect ratio and radius and it is not easy to derive an analytical expression for the purposes of this project, which is why we relate to simulations.

2.2 Opacity

The opacity within protoplanetary discs is mainly determined by dust. The sublimation of silicates requires very high temperatures (T $\gtrsim$ 1500 K), which means that only in the innermost parts of the disc the dust particles could be destroyed leaving only the gas molecular opacity. In general, the opacity of a medium is a measurement of its impenetrability to radiation, describing its absorption or scattering from that medium. A beam of light traversing a medium gets attenuated; this is called extinction. The extinction of light within a protoplanetary disc is caused by absorption and scattering due to the spherical dust particles (van de Hulst, 1957; Bohren & Huffman, 1983). Scattering is caused by inhomogeneities in the medium through which light travels, which in this case is gas. Any material has inhomogeneities because the molecules it consists of act as scattering centres, but their arrangement defines the efficiency of scattering. Dust grains are considered to be sufficiently distant so that scattering due to one particle does not affect the other ones. In the following multiple scattering will be neglected. The medium can also absorb all or part of the incident light. Then energy is transferred from the beam to the material and the intensity of the light is reduced. The opacity of a medium, thus, describes the amount of extinction caused to a beam of light when it passes through it and extinction depends on its material properties and the wavelength of the incident light. Therefore in each case of radiation through a medium the electromagnetic wave can be absorbed, scattered or

both. The intensity of radiation travelling through a medium will change as a function of the distance travelled x

$$\frac{dI_\lambda}{dx} = -\kappa_\lambda \rho I_\lambda \tag{2.23}$$

and if we integrate this equation we get that the radiation intensity which can be described as

$$I_\lambda = I_{0,\lambda} e^{-\kappa_\lambda \rho x} . \tag{2.24}$$

The wavelength dependent opacity κ_λ consequently affects the difference between the radiation the medium absorbs to what was emitted from the source. We can also define the optical depth which is

$$\tau_\lambda = \int_\infty^0 \kappa_\lambda \rho \, dx \tag{2.25}$$

and write

$$I_\lambda = I_{0,\lambda} e^{-\tau_\lambda} . \tag{2.26}$$

Based on the amount, size, structure and the composition of the dust particles the disc can be optically thin or thick. An optically thin disc ($\tau_\lambda < 1$) lets light pass through it without absorption and it emits radiation proportionally to the emitting area of the particles, whereas in an optically thick disc that absorbs all or part of the incident light, the emission is proportional to the surface area of disc. Opacity is a very important factor of a protoplanetary disc since it defines its observational characteristics, either on the thermal continuum emission or by affecting the density structure and the temperature which produces different excitation conditions for the gas lines.

The wavelength dependent opacities κ_λ for dust particles can be calculated through Mie theory, which describes the extinction of an electromagnetic plane wave by a homogeneous, isotropic sphere. More specifically, the wavelength dependent opacity can be written as (Movshovitz & Podolak, 2008)

$$\kappa_\lambda = \frac{\sigma_\lambda n_{gr}}{\rho_g} \tag{2.27}$$

or

$$\kappa_\lambda = \frac{Q_e(x)\pi s^2 n_{gr}}{\rho_g} , \tag{2.28}$$

if we substitute the effective cross-section, $\sigma_\lambda = Q_e \pi s^2$, of a spherical dust grain. Here Q_e is the extinction efficiency and $x = 2\pi s/\lambda$ the size parameter. The number density of grains is given by $n_{gr} = f_{DG}\rho_g/m_{gr}$, where m_{gr} is the grain mass, f_{DG} is the dust-to-gas ratio, ρ_g is the gas density and s is the grain size [1].

The extinction efficiency is

$$Q_e = \frac{C_e}{\pi s^2} = \frac{W_e}{I_i \pi s^2} , \tag{2.29}$$

---

[1]See Appendix A for plots of the wavelength dependent opacities as a function of x for different grain sizes

with W_e the rate at which the electromagnetic energy is lost due to extinction and I_i the incident irradiance. The extinction coefficient is a sum of the absorption and scattering coefficient so it can be expressed as (van de Hulst, 1957, p.128)

$$Q_e = Q_a + Q_s \ . \tag{2.30}$$

When scattering is neglected then $Q_e = Q_a$.

The absorption and scattering efficiencies can be expressed in the same way as the extinction efficiency in Equation 2.29, but they can also be approximated as (Movshovitz & Podolak, 2008)

$$Q_a = \frac{24xn_r n_i}{(n_r^2 + 2)^2} \ , \tag{2.31}$$

$$Q_s = \begin{cases} \frac{8x^4}{3} \frac{(n_r^2-1)^2}{(n_r^2+2)^2}, & \text{for } x < 1.3 \\ 2x^2(n_r - 1)^2(1 + \left(\frac{n_i}{n_r-1}\right)^2), & \text{for } x \geq 1.3 \end{cases} \ . \tag{2.32}$$

In these expressions n_r,n_i are the real and imaginary part of the particle's refractive index. In these expressions we can see the connection of the opacity with the size parameter x and its refractive index. However, in this thesis this approximation will not be used. Instead, the RADMC-3D code will be used (see Chapter 3.1) to calculate the mean opacities using Equation 2.28 and 2.34 to 2.36 for the averaged opacities (see also Appendix A).

In the energy equations (Equations 2.16 and 2.17) of the hydrodynamical simulation presented here, we use the mean opacities that are averaged over all wavelengths. Below, the Rosseland and Planck mean opacities will be introduced, along with the stellar opacities. The Planck black body radiation energy density distribution describes the amount of energy that a body emits per unit area of the body, per unit solid angle that the radiation is measured over as, at a given wavelength λ and temperature T

$$B_\lambda(\lambda, T) = \frac{2hc^2}{\lambda^5} \frac{1}{e^{\frac{hc}{\lambda k_B T}} - 1} \ , \tag{2.33}$$

with h the Planck constant, k_B the Boltzmann constant and c the speed of light. If we use $B_\lambda(\lambda, T)$ as a weighting function we can define the Planck mean opacity as

$$\kappa_P = \frac{\int_0^\infty \kappa_{\lambda,ns}(T,\rho)B_\lambda(\lambda,T)d\lambda}{\int_0^\infty B_\lambda(\lambda,T)d\lambda} \ . \tag{2.34}$$

Since the mean free path of thermal radiation in the disc is small compared to the disc's scale height, the radiation field can be considered isotropic, blackbody emission. The radiation flux is connected to the gradient of the energy density by the Rosseland mean opacity κ_R as shown in the previous section. The Rosseland mean opacity uses the temperature derivative of the Planck distribution as a weighting function and is defined as

$$\kappa_R^{-1} = \frac{\int_0^\infty \kappa_{\lambda,s}^{-1}(T,\rho)(\partial B_\lambda(\lambda,T)/\partial T)d\lambda}{\int_0^\infty (\partial B_\lambda(\lambda,T)/\partial T)d\lambda} \ . \tag{2.35}$$

It should be noted that scattering processes are neglected (subscript ns) when calculating the wavelength dependent opacities κ_λ for the Planck mean, but are included in the Rosseland mean opacity (subscript s).

Both of these mean opacities take into account the local temperature of the disc. We can also consider the stellar radiation and define the stellar or optical opacity

$$\kappa_\star = \frac{\int_0^\infty \kappa_{\lambda,ns}(T,\rho) J_\lambda(T_\star) d\lambda}{\int_0^\infty J_\lambda(T_\star) d\lambda} \tag{2.36}$$

Here we can approximate the mean intensity of the star's radiation as $J_\lambda(T_\star) = B_\lambda(T_\star)$, assuming that it is isotropic. The stellar opacity is then the Planck mean opacity taking into consideration the stellar radiation temperature instead of the local disc temperature. This is the mean opacity used when calculating the stellar heating component of the radiation energy evolution equation and therefore it will not be used in this project.

2.3   Dust grain dynamics

In order to understand the size distribution of particles in a disc, we must understand how these particles grow and fragment. The collision between two dust grains can result in various outcomes. Let us assume that one of the bodies is the impactor and the other one is the target. The possible outcomes are coagulation, fragmentation, cratering and bouncing (review by Blum & Wurm, 2008). Coagulation or sticking means that all of the mass from the impactor becomes part of the mass of the final body that also includes all the initial mass of the target body. Fragmentation or shattering means that the collision fragments the target into two or more pieces, thus replenishing the small grains. The outcome is cratering or erosion when the impactor excavates part of the target's mass and finally if the two bodies bounce they only change their initial directions without mass transfer.

The outcome of a collision is determined by the mass difference between the colliding bodies and their relative velocities. The fragmentation probability (Birnstiel et al., 2010) is

$$p_f = \begin{cases} 0 & \text{if} \ \ \Delta u \ll u_f - \delta u \\ 1 & \text{if} \ \ \Delta u \geq u_f \ . \\ 1 - \frac{u_f - \Delta u}{\delta u} & \text{else} \end{cases} \tag{2.37}$$

Here, Δu is the relative velocity of the two bodies and u_f the fragmentation threshold, above which collisions result to fragmentation. It has been found in laboratory experiments that there is not a sharp threshold, but rather a region of transition with a width $\delta u = 0.2 u_f$ (Blum & Münch, 1993).

Additionally, the mass ratio determines if the collision will result in complete fragmentation of the larger body or if it will result in cratering. The above description assumes that all bodies have constant porosity and their composition is accounted for only by a

difference in the fragmentation velocity thresholds. Typical values are $u_f \sim 1 \ m/s$ for silicates (Poppe et al., 2000) and $u_f \sim 10 \ m/s$ for icy particles (Gundlach & Blum, 2015).

The relative velocities between grains are determined by the grain sizes, but they are also greatly affected by the local temperature and the gas scale height. Dust dynamics involve not only collisions between grains, but also with the molecules of the protoplanetary disc's gas. These collisions with gas cause a lag to the dust particles that leads to relative velocities between themselves. Then, the respective velocities of colliding dust particles will define the outcome (Weidenschilling, 1977, 1980; Blum & Wurm, 2008, and references therein). Grains of small sizes will stick together and form larger ones, but as these particles grow it becomes more likely that they could also bounce and no mass is lost or transfered (Blum & Münch, 1993). Larger grains that collide, fragment into smaller particles and cratering or erosion can happen when small grains collide with large ones. Consequently, as collisions are expected to naturally occur in protoplanetary discs, it is also expected that there will be several different dust sizes changing as the disc evolves. It is, hence, important to know the number density of these particles at each position within the disc.

We assume that the different sources of the relative velocities between dust grains are Brownian motion, turbulence, azimuthal and radial drift depending on the size of the grains (Birnstiel et al., 2011). The relative velocities between two small particles of masses m_1 and m_2 due to Brownian motion are

$$\Delta u_{BM} = \sqrt{\frac{8k_B T(m_1 + m_2)}{\pi m_1 m_2}} \ . \tag{2.38}$$

k_B is the Boltzmann constant and T the gas temperature. Those particles are very small (around micrometre-sized), so that they have random motions due to collisions with the gas molecules.

When the size of the particles increases, turbulent motions of the gas start to affect them. If we consider homogeneous and isotropic turbulence, then it is characterized by a cascade of energy through a range of scales from the largest spatial scale or largest eddy to the smallest scale or eddy, where it is dissipated. The aforementioned eddies are localized flow structures and it is assumed that mass and kinetic energy are conserved while they break into smaller structures, until they are wiped out due to viscous friction (Richardson, 1922). Turbulent mixing for larger grains can be separated into two different regimes. In the first one, the smaller particles of the regime, or more specifically those with a smaller stopping time than the eddy crossing time have relative velocities proportional to

$$\Delta u_I \propto |St_1 - St_2| \ , \tag{2.39}$$

where St_1 , St_2 are the Stokes numbers of the particles (Ormel & Cuzzi, 2007). These particles are coupled to the gas. The relative velocities of the larger particles, which get decoupled from the gas, follow the expression

$$\Delta u_{II} \propto \sqrt{St_{max}} \ , \tag{2.40}$$

where St_{max} is the Stokes number of the largest particles. These relative velocities between particles then define the outcome of collisions.

The Stokes number of dust particles suspended in gas is defined as the product of the particle stopping or friction time and the Keplerian angular velocity,

$$St = \tau_f \Omega_K \tag{2.41}$$

and it describes the aerodynamical properties of a dust particle or in other words, how well it is coupled to the gas. The stopping or friction time is the time it takes a dust particle to decelerate due to gas drag and in the Epstein regime it is defined as

$$\tau_f = \frac{m\Delta u}{|F_D|} \, , \tag{2.42}$$

for particles of size s, volume density ρ_s and mass $m = (4/3)\pi s^3 \rho_s$. Here F_D is the drag force in the Epstein regime which describes the movement of the dust particle within the gas when the radius of the dust sphere is smaller compared to the mean free path of the gas molecules. (Whipple, 1972; Weidenschilling, 1977) It is also based on the assumptions that the velocities of the gas molecules follow Maxwell's distribution law and the velocity of the dust sphere is small. In the former case, the velocity components of the gas particles normal to the sphere's surface are reversed after the collision, while in the latter they are random. In the Epstein regime the drag force is

$$|F_D| = \frac{4\pi}{3}\rho_g s^2 u_{th}\Delta u, \tag{2.43}$$

where u_{th} is the mean thermal speed of molecules and ρ_g is the gas volume density. The stopping time becomes

$$\tau_f = \frac{\rho_s s}{\rho_g u_{th}} \, . \tag{2.44}$$

The mean thermal speed is connected to the sound speed since

$$u_{th} = \sqrt{\frac{8k_B T}{\pi \mu m_p}} \tag{2.45}$$

and

$$c_s = \sqrt{\frac{k_B T}{\mu m_p}} \, . \tag{2.46}$$

m_p is the proton mass and $\mu = 2.3$ is the mean molecular weight in proton masses. The Stokes number is then

$$St = \sqrt{\frac{\pi}{8}} \frac{\rho_s s}{c_s \rho_g}\Omega_K \tag{2.47}$$

Using Eq.(2.10) or $\Omega_K = \frac{c_s}{H_g}$ the above expression is

$$St = \sqrt{\frac{\pi}{8}} \frac{\rho_s s}{\rho_g H_g} \, . \tag{2.48}$$

At midplane, where $\rho_g = \rho_{g,0}$ we can use Equation 2.9, so that the Stokes number at midplane is given by

$$St = \frac{\pi}{2} \frac{\rho_s s}{\Sigma_g} \ . \tag{2.49}$$

Another factor that contributes to the dust composition and dynamics is condensation. Water-ice particles will sublimate when they cross the iceline and there is also a temperature that for example silicates sublimate, but this is considered so high ($T \geq 1500K$) that it is not reached in most of the cases in protoplanetary discs. It is also important to consider that the temperature at which water-ice sublimates is also defined by pressure. The opacity caused by dust grains changes at the iceline (Figure 3.1), because the icy mass fraction sublimates across the iceline and therefore no longer contributes to the opacity. As a first approximation I will use grains of single composition and constant porosity. More specifically, the grains used in this project are 50% pure H_2O and 50% are pure silicate. Inside the iceline the icy particles are removed. This prescription is a simplification. In reality, particles may be layered with icy coatings. Furthermore, recondensation of vapour may facilitate growth, while sublimation may release small silicate grains (Ros & Johansen, 2013; Schoonenberg & Ormel, 2017). This effect is ignored in this project. An additional factor of dust dynamics in gas is radial drift which along with fragmentation provides a limitation to the maximum grain size possible. The disc is hotter and denser close to the star and the gas has a sub-Keplerian speed due to the radial pressure gradient force. The particles do not feel the pressure gradient force so they have Keplerian velocity, but they experience the gas drag force from the sub-Keplerian gas and thus experience a radial drift speed towards the star (Weidenschilling, 1977) which is

$$v_{drift} = -\frac{2\Delta u_\eta}{St + St^{-1}} \ , \tag{2.50}$$

where in this case Δu_η is the velocity difference between the orbital velocity of the dust particles V_k and the gas speed v_{gas} or $\Delta u_\eta = V_k - v_{gas} = \eta V_k$. This is given by

$$\Delta u_\eta = -\frac{1}{\rho} \frac{dP}{dr} \frac{r}{2V_K} \ . \tag{2.51}$$

Using Equation 2.5 we find

$$\Delta u_\eta = -\frac{c_s^2}{2V_K} \left| \frac{d \ln P}{d \ln r} \right| \tag{2.52}$$

We can see from the above expressions that the maximum drift speed is for $St = 1$ and by substituting typical values we find that the corresponding particle size is around 1 cm. The time scale for drift is

$$\tau_{drift} = \frac{r}{v_{drift}} \tag{2.53}$$

so approximately a few hundred years for centimetre-sized particles at 5 AU. There is also the fragmentation barrier that limits grain growth. It can be shown that the fragmentation

barrier is lower than the radial drift barrier and consequently particles fragment before they are entirely swept up (see Figure 2.2).

The Stokes number of the largest possible particle size can be found by equating the relative velocity induced by turbulent motion $\Delta u = \sqrt{3\alpha St} c_s$ (Ormel & Cuzzi, 2007) and the fragmentation velocity u_f as in Birnstiel et al. (2009)

$$St_{fragm} \simeq \frac{1}{3} \frac{u_f^2}{\alpha c_s^2} \ . \tag{2.54}$$

Using also the Stokes number from Equation 2.48 we can find the maximum particle size due to fragmentation

$$s_{fragm} \simeq \frac{2}{3} \sqrt{\frac{2}{\pi}} \frac{\rho_g H_g}{\rho_s \alpha} \frac{u_f^2}{c_s^2} \ . \tag{2.55}$$

We can calculate the maximum particle size at midplane using Equation 2.9

$$s_{fragm,0} \simeq \frac{2}{3\pi} \frac{\Sigma_g}{\rho_s \alpha} \frac{u_f^2}{c_s^2} \tag{2.56}$$

at an order of magnitude or

$$s_{fragm,0} = f_f \frac{2}{3\pi} \frac{\Sigma_g}{\rho_s \alpha} \frac{u_f^2}{c_s^2} \ , \tag{2.57}$$

where the constant $f_f = 0.37$, found through numerical simulations (Birnstiel et al., 2012)

In order to estimate the limit to the particle size due to radial drift we have to consider the time it takes for drift to remove particles and the growth time scale. The time scale at which particles coagulate can be found through (Kornet et al., 2001)

$$\dot{s} = \frac{\rho_d}{\rho_s} \Delta u = \frac{\rho_d}{\rho_s} \sqrt{3\alpha St} \ c_s \ . \tag{2.58}$$

Following Brauer et al. (2008) the growth time is

$$\tau_{grow} = \frac{s}{\dot{s}} \Rightarrow \tag{2.59}$$

$$\tau_{grow} \simeq \sqrt{\frac{St}{\alpha}} \frac{\rho_g}{\rho_d} \frac{1}{\Omega_K} \ . \tag{2.60}$$

We assume that the dust scale height it is related to the gas scale height (Youdin & Lithwick, 2007)

$$H_{dust} = H_{gas} \sqrt{\frac{\alpha}{St}} \quad \text{for} \quad St > \alpha \ . \tag{2.61}$$

Using Equation 2.61 and considering again the midplane values so that we can also use Equation 2.9 the growth time is

$$\tau_{grow} \simeq \frac{1}{\Omega_K f_{DG}} \ , \tag{2.62}$$

where $f_{DG} = \Sigma_d / \Sigma_g$ is the dust-to-gas ratio.

Following Equation 2.53 and substituting Equation 2.50 we find

$$\tau_{drift} = \frac{r V_K (St^{-1} + St)}{c_s^2 \gamma} \ , \tag{2.63}$$

with $\gamma = \left| \frac{d \ln P}{d \ln r} \right|$ the pressure gradient. The pressure gradient can be written as $\gamma = |-p - q/2 - 3/2|$ if we assume that $\Sigma \propto r^{-p}$ and $T \propto r^{-q}$, with p and q constants. The above expression can then be approximated as

$$\tau_{drift} \simeq \frac{r V_K}{St \ c_s^2} |-p - q/2 - 3/2|^{-1} \ , \tag{2.64}$$

considering that for $St < 1$, $St^{-1} + St \approx St^{-1}$.

By equating the growth and the drift time scales (Eq.(2.60) and (2.64)) we find that the maximum Stokes number that can be reached before the grains are lost by radial drift is

$$St_{drift} = f_d \frac{V_K^2}{c_s^2} f_{DG} \gamma^{-1} \tag{2.65}$$

with a corresponding grain size in this case at midplane

$$s_{drift,0} = f_d \frac{V_K^2 \Sigma_d}{c_s^2 \rho_s} \gamma^{-1} \tag{2.66}$$

or

$$s_{drift,0} = f_d \frac{\Sigma_d}{\rho_s \gamma} \left(\frac{H}{r} \right)^{-2} \ , \tag{2.67}$$

since $V_K = \Omega_K \cdot r$. The constant $f_d = 0.55$ was again found through numerical simulations (Birnstiel et al., 2012)

We can calculate the maximum grain sizes for the fragmentation barrier (Equation 2.57 and 2.66) for typical values used in the protoplanetary disc simulations of this project. In Figure 2.2 we see the fragmentation barrier for different fragmentation threshold velocities (u_f) and α-viscosity parameters compared to the radial drift barrier. These grains size limits were calculated for a dust-to-gas ratio of 0.01 and a surface density profile $\Sigma \propto r^{-\frac{1}{2}}$. However in order to calculate the drift barrier we also need the temperature profile of the disc. In the hydrodynamical code used for the simulations of this project, the power-law index is not constant, but is evolving. Therefore, for simplicity, the drift barrier was

calculated using the temperature profile at the beginning of the simulation (1/10 of an orbit) which was $T \propto r^{-\frac{1}{2}}$.

We can see in Figure 2.2 that the fragmentation barrier decreases with increasing α-viscosity parameter, which is expected, since an increased α leads to increased turbulent relative velocities. Moreover, the maximum possible grain size decreases when the threshold velocity decreases. The fragmentation barrier is lower than the radial drift barrier for all the different values of u_f and α which means that fragmentation dominates for the disc setup in this project. Particles will fragment before they drift all the way to the star and thus replenish the small particles (Birnstiel et al., 2015). The small particles are less affected by radial drift as it can be seen by Equation 2.50 and since they coagulate, an equilibrium forms that drives the grain size distribution. The above conclusions do not mean that drift is not present or significant in protoplanetary discs, but given the sizes and the parts of the disc considered in this project, we can neglect drift and assume that only fragmentation is responsible for the largest possible grain size.
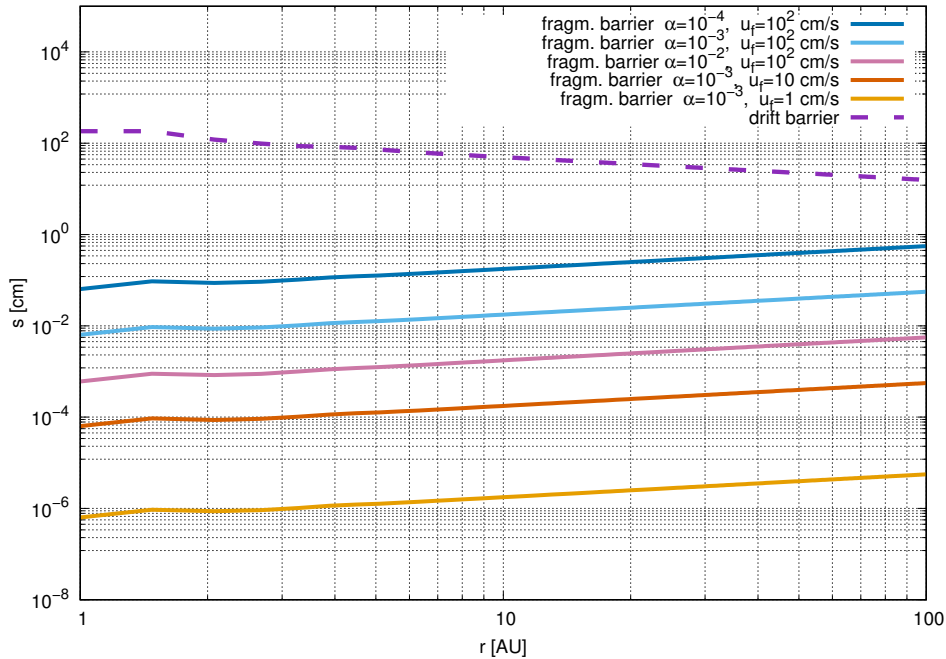
Figure 2.2: Maximum possible grain sizes due to fragmentation and radial drift for $u_f = 1, 10, 100 cm/s$, $\alpha = 10^{-2}, 10^{-3}, 10^{-4}$ and $f_{DG} = 10^{-2}$. The surface density profile follows $\Sigma \propto r^{-\frac{1}{2}}$ and the temperature profile at the start of the simulation follows $T \propto r^{-\frac{1}{2}}$. The fragmentation barrier calculated using the disc parameters that will be used in the models of this project and for multiple fragmentation velocities and α-viscosity parameters. The drift barrier is higher compared to all the fragmentation barrier calculations considered.

Another effect on the dust particles is settling that affects sufficiently large grains,

causing them to concentrate towards midplane. The settling timescale is

$$t_{sett} = \frac{z}{u_{sett}} \ .$$ (2.68)

The speed at which particles settle u_{sett} can be found by equating the vertical gravity component with the gas drag. The vertical component of gravity is

$$F_{grav} = mg_z$$ (2.69)

and substituting Equations 2.4 and 2.12

$$F_{grav} = m\Omega_K^2 z \ ,$$ (2.70)

while gas drag was introduced in Equation 2.43. Consequently the settling speed is

$$u_{sett} = \frac{\Omega_K^2}{u_{th}} \frac{\rho_s s z}{\rho_g(z)}$$ (2.71)

and the timescale can be written (using Eq. 2.44 and 2.48)

$$t_{sett} = \frac{1}{St\Omega_K}$$ (2.72)

which means that the larger the dust particle the faster it settles. Not only the size, but the location of the particle within the disc matters, because the time increases with increasing orbital distance and the Stokes number depends on the gas density as well. At high z above the midplane, the gas density is low which means that these regions are more easily depleted. But particles do not reach immediately the midplane as turbulence can diffuse them upwards (Whipple, 1972; Weidenschilling, 1977; Armitage, 2009, for an overview).

The timescale for vertical diffusion is

$$t_{diff} = \frac{z^2}{\nu} \ ,$$ (2.73)

where we use viscosity ν as the turbulent diffusion coefficient. Considering Equation 2.14 we can estimate the turbulence required in order to oppose settling by equating the settling and diffusion timescales and considering that dust will start settling below H_g

$$\alpha \leq \frac{H_g^2 \Omega_K St}{c_S^2} \ .$$ (2.74)

Using Equation 2.10 we find that turbulence must be $\alpha \lesssim St$ for settling to become important (Armitage, 2009). This can also be seen from Equation 2.61 which relates the gas scale height to the dust scale height.

2.3.1 Grain size distributions

The consequence of dust grain dynamics, fragmentation coagulation or, for example, erosion lead to a size distribution within a protoplanetary disc that evolves as these dynamics come into play. As a first approach, a steady-state mass distribution of grain sizes due to fragmentation can be written as a power-law (Dohnanyi, 1969; Tanaka et al., 1996).

$$n(m)dm = C'm^{-\xi}dm \; , \tag{2.75}$$

with $n(m)$ the number density of grains as a function of their mass m and C',ξ constants. In several studies it has been shown that $\xi = \frac{11}{6}$ (Dohnanyi, 1969; Mathis et al., 1977; Williams & Wetherill, 1994; Paolicchi, 1994; Tanaka et al., 1996). We can then convert that to a size distribution considering that $m \propto s^3$ for ρ_s=const., where s is the particle size and ρ_s the particle's density.

$$n(m)dm = Cs^{-3\alpha}ds^3 \tag{2.76}$$
$$= Cs^{2-3\alpha}ds \; . \tag{2.77}$$

Usually when it comes to the grain size distribution in circumstellar discs, we adopt a power law for the number density of the particles as described above. Nevertheless, this power-law distribution has been found not to agree with the results when both fragmentation and cratering occur in the dust particles of a circumstellar disc . For this project the recipe by Birnstiel et al. (2011) has been followed to produce a more complex grain size distribution. This distribution starts with the same power-law, with ξ=11/6. However, it has been proposed in Birnstiel et al. (2011) that in order to create a realistic grain size distribution, considering grain growth and grain dynamics, one power law is not sufficient. Instead the distribution is constructed using several power laws that depend on the grain size. The details of this recipe are discussed in more detail in Chapter (3). Both of the aforementioned models will be tested in this project, the simple power-law of Equation 2.77 and the more complex model of Birnstiel et al. (2011).

Taking a look again at Figure 1.2, we can see that the next step, after determining the particle sizes, is to determine the opacities. The total opacity of the disc at each location is dominated by the amount of dust, the sizes of those grains, so the grain size distribution, but also their structure and composition. The cooling rate is inversely proportional to the opacity

$$Q^- \propto \frac{1}{\kappa\rho} \; , \tag{2.78}$$

which means that temperature will then change and according to the hydrostatic equilibrium the aspect ratio will change accordingly. So if for example the opacity increases, then the cooling rate decreases, the disc gets hotter and the aspect ratio becomes larger. This means that the gas scale height increases and by Equation 2.14 so does the viscosity assuming α is constant. If we consider constant accretion rate (Equation 2.15), then the surface density of the disc will decrease, affecting the density profile and so on, so forth.

Chapter 3

Methodology

3.1 Opacity-Temperature relation

As a first step in this project I am using the RADMC-3D code (Dullemond, C. P. et al., 2012, http://www.ita.uni-heidelberg.de/~dullemond/software/radmc-3d/), which is a radiative transfer code that can be used to simulate observational data, such as the spectrum of a geometric distribution of gas and dust. Part of the code uses Mie theory (relevant calculations were introduced in Chapter 2.2) in order to calculate the opacity of grains as a function of temperature. For the purposes of this project, this part of the code will be used.

The main input parameters are the size of the grains and the dust-to-gas ratio. We can also choose the dust grain species, silicates, water ice and carbon or the fraction between those in the dust mixture. In Figures 3.1, 3.2 we can see how each opacity scales with temperature for five different grain sizes, from 0.1 micrometre to 1 millimeter. The mixture chosen for this project is 50% silicates and 50% ice and the disc dust-to-gas ratio is 1%. Both of these parameters can be probed to create different initial disc structures, in order to test how different grain species, such as water-ice and silicates, evolve and to see what is the role of the fraction between them in the disc's structure (Bitsch & Johansen, 2016). Moving back to the input parameters, the temperature grid should be specified (how many temperature values and within which boundaries) and then, using the input parameters mentioned before, an opacity file is created that corresponds to a given grain size and contains the mean Rosseland and Planck opacities as a function of temperature.

The mathematical expressions for the wavelength dependent opacities κ_λ mentioned in Chapter (2.2) may be misleading when trying to analyse Figure 3.1. It is important to note that the extinction coefficient Q_e and therefore κ_λ is not only a function of $x = \frac{2\pi s}{\lambda}$, but also of the refractive index $m = n_r + in_i$, which is also dependent on wavelength and on the grain composition[1]. We can see in Figure 3.1 that the Rosseland mean opacities

---

[1]The n_r and n_i refractive index components used in RADMC-3D are plotted in Figure A.1 as a function
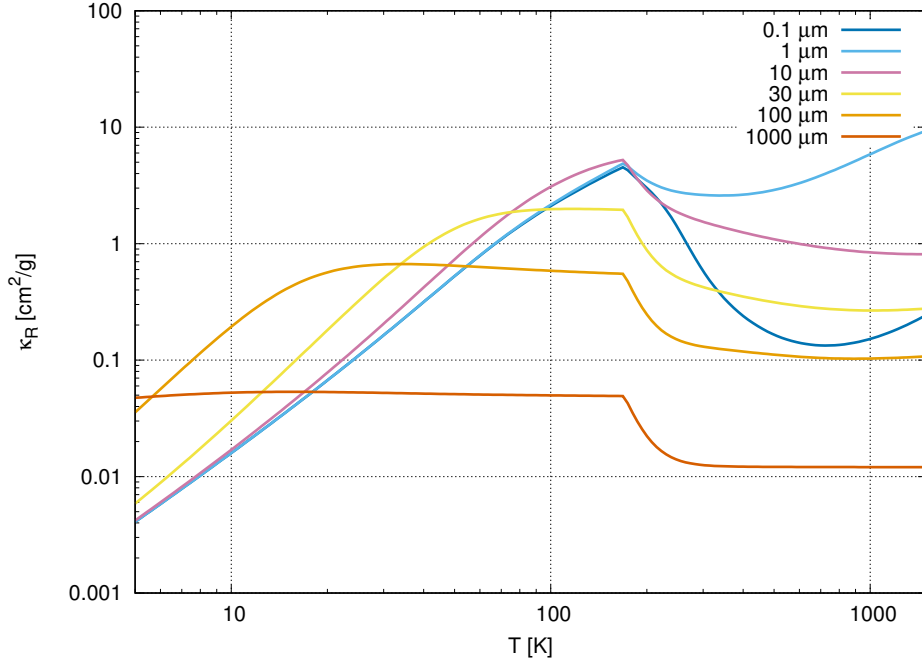
Figure 3.1: Rosseland mean opacity as a function of temperature for six different grain sizes. These values were calculated using RADMC-3D for a mixture of 50% silicates, 50% ice and disc dust-to-gas ratio of 1%.

for the largest particles of the set (100 and 1000 μm) are almost flat, except for the transition around the iceline at 170 K. At this temperature, ice sublimates and the opacity is then only determined by silicates. For large particle sizes, the geometry of the particles dominates over scattering and the mean opacity is independent of temperature. Using the size parameter $x = 2\pi s/\lambda$ we find that the regime changes at approximately $x = 1$ and more specifically at $x \ll 1$ we have the Rayleigh scattering, whereas at $x \gg 1$ we have the geometric optics regime. Consequently, if the size of the particle is a lot smaller than the wavelength of the incident radiation, absorption dominates over scattering and

$$Q_e(x) \propto x \ . \tag{3.1}$$

In the case of the larger grain sizes, or when $x \gg 1$, $Q_e(x)$ is approximately constant and specifically $\lim_{x \to \infty} Q_e(x) = 2$ (see Figure A.3) in Appendix A). This leads to the paradox that a large particle removes twice the incident energy (Bohren & Huffman, 1983). The paradox is solved by considering that at this limit the geometric optics should be combined with scalar diffraction theory and eventually it has been found that the extinction cross section C_e (Equation 2.29) is twice the area of the object. While all of the incident energy is absorbed by the particle, the edges also scatter an equal amount of energy, or in other words the extinction of the incident electromagnetic wave is influenced beyond the physical boundaries of the particle.

---

of wavelength (Jaeger et al., 1994; Dorschner et al., 1995; Warren & Brandt, 2008).
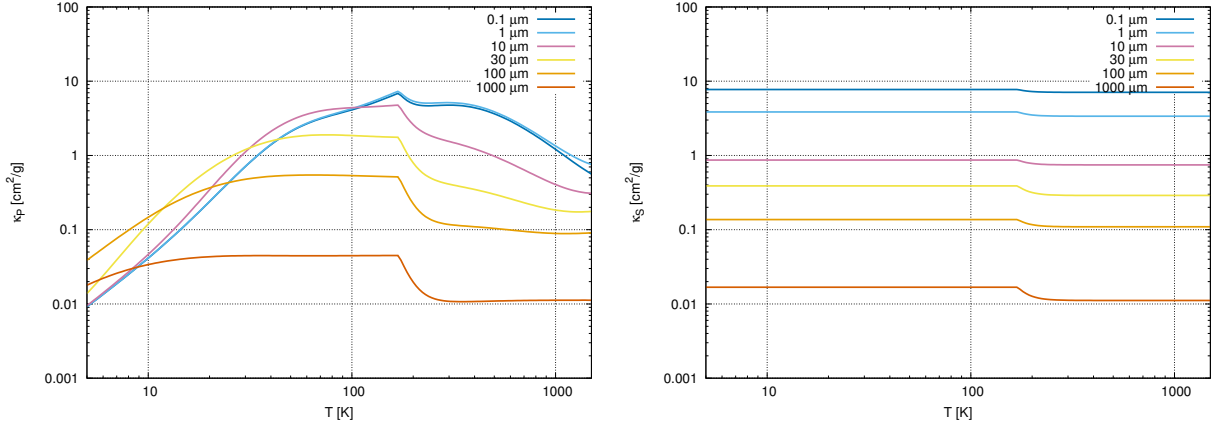
Figure 3.2: The left plot is the Planck mean opacity as a function of temperature for 5 different grain sizes. The right figure is the stellar or optical mean opacity as a function of temperature for the same grain sizes. These values were calculated using RADMC-3D for a mixture of 50% silicates, 50% ice and disc dust-to-gas ratio of 1%. for 5 different grain sizes.

In order to explain the Rosseland mean opacities as a function of temperature (Figure 3.1) we can substitute n_{gr} and $m_{gr} = 4\pi\rho_{gr}s^3$ so that Equation 2.28 is simplified to

$$\kappa_\lambda = \frac{Q(x)f_{DG}}{4\rho_{gr}s} \tag{3.2}$$

For the larger particles, $s = 100$ and 1000μm, the wavelength dependent opacity has a constant extinction coefficient and is therefore independent of the temperature. For the small particles $s = 0.1, 1$ and 10μm, considering that $Q_e \propto 2\pi s/\lambda$ and by Wien's displacement law

$$\lambda_{max} = \frac{b}{T} \ , \tag{3.3}$$

with $b \approx 2900$ μm K, we get

$$\kappa_\lambda \propto \frac{\pi f_{DG}}{2\rho_{gr}\lambda} \propto T \ , \tag{3.4}$$

so the wavelength dependent opacity is proportional to the temperature, but independent of the grain size. We can also see in Figure 3.1 that the mean Rosseland opacity values for the 100 μm grains are not constant at low temperatures. This happens because for temperature $T \leq 30$K we have $x \lesssim 6$, so opacity is still dependent on wavelength and consequently temperature (see Figure A.3).

At $T = 170$ K the ice sublimates and opacity is determined only by the silicates. Additionally, the different grain sizes have a different value of x at which ice sublimates and we can explain their profiles beyond the iceline following the approximate values of Equation A.2 in Appendix A.

We see in Figure 3.2 that the Planck opacities have a weaker dependency on temperature compared to the Rosseland mean opacities. The stellar opacities are only dependent in the stellar temperature, showing only the decrease in opacity across the iceline as described above. Both the Planck and stellar opacities are calculated using only the absorption coefficient, which has does not have a strong dependency on wavelength and consequently temperature, as opposed to the extinction coefficient. The Planck mean opacities are calculated taking into account the temperature of the disc, while the stellar opacities, use the temperature of the star, which is constant.

3.2 Grain size distribution

3.2.1 A full grain size distribution model

The next step is to test the effect that several grain sizes have on the structure and evolution of a protoplanetary disc. The largest bodies of the distribution reach velocities higher than their fragmentation threshold and shatter into smaller pieces. The same happens to those fragments until small particles of around micrometre sizes are created. Dust particles in protoplanetary discs collide and stick together forming larger grains. The equilibrium between these two processes, fragmentation and coagulation, results in a steady-state size distribution, where the number density of the particles can be written as $n(m)dm = C'm^{-\xi}dm$ or $n(s)ds = Cs^{2-3\xi}ds$, with m the particle mass, s the particle size and ξ a constant. The constants are connected through

$$C = 3C' \left(\frac{4\pi}{3} \rho_s \right)^{1-\xi} \tag{3.5}$$

since $m = \frac{4\pi}{3} \rho_s s^3$.

The mass of a specific size, within a size bin $[s_i - ds', s_i + ds'']$ is

$$M_{s_i} = \int_{s_i-ds'}^{s_i+ds''} m \cdot n(s)ds \tag{3.6}$$

$$= \frac{4\pi}{3} \rho_s C \left[\frac{s^{6-3\xi}}{6-3\xi} \right]_{s_i-ds'}^{s_i+ds''} , \tag{3.7}$$

assuming 5-3$\xi \neq$ -1. The grain sizes for this project are distributed over a logarithmic grid, so $s_i - ds'$ is $\sqrt{s_i \cdot s_{i-1}}$ and $s_i + ds''$ is $\sqrt{s_i \cdot s_{i+1}}$.

The constant C can be found by the total mass M_{tot} present in an annulus.

$$M_{tot} = \int_{m_0}^{m_n} mn(m)dm \tag{3.8}$$

$$= C' \left[\frac{m^{2-\xi}}{2-\xi} \right]_{m_0}^{m_n} \quad \Rightarrow \tag{3.9}$$

$$M_{tot} = \frac{C'}{2-\xi}(m_n^{2-\xi} - m_0^{2-\xi}) \tag{3.10}$$

so we can write

$$C' = \frac{(2-\alpha)M_{tot}}{m_n^{2-\alpha} - m_0^{2-\alpha}} \ , \tag{3.11}$$

where m_n and m_0 are the masses of the largest and the smallest grain size in the grid cell respectively.

The total mass M_{tot} present in an annulus is an integration of the dust surface density Σ_d over the area of the annulus.

$$M_{tot} = \int_{A_{in}}^{A_{out}} \Sigma_d \ dA \tag{3.12}$$

so since in a grid cell $\Sigma_d = f_{DG} \cdot \Sigma_g$

$$M_{tot} = \int_{A_{in}}^{A_{out}} f_{DG}\Sigma_g dA \tag{3.13}$$

$$= 2\pi f_{DG}\Sigma_g \int_{r_{in}}^{r_{out}} rdr \Rightarrow \tag{3.14}$$

$$M_{tot} = \pi f_{DG}\Sigma_g(r_{out}^2 - r_{in}^2), \tag{3.15}$$

where f_{DG} is the disc's dust-to-gas ratio, r_{in}, r_{out} the inner and outer boundary of the grid cell. Therefore,

$$C' = \frac{(2-\alpha)\pi f_{DG}\Sigma_g(r_{out}^2 - r_{in}^2)}{m_n^{2-\alpha} - m_0^{2-\alpha}} \tag{3.16}$$

The constant C' is connected to C as in Equation 3.5, conseqently

$$C = \frac{3\pi f_{DG}\Sigma_g(2-\alpha)\left(\frac{4\pi}{3}\rho_s\right)^{1-\alpha}\left(r_{out}^2 - r_{in}^2\right)}{m_n^{2-\alpha} - m_0^{2-\alpha}} \tag{3.17}$$

and the mass around a grain size s_i is then

$$M_{s_i} = \left(\frac{4\pi}{3}\rho_s\right)^{-\xi} \frac{\pi(r_{out}^2 - r_{in}^2)}{m_n^{2-\xi} - m_0^{2-\xi}} f_{DG}\Sigma_g \left[(\sqrt{s_i \cdot s_{i+1}})^{6-3\xi} - (\sqrt{s_i \cdot s_{i-1}})^{6-3\xi} \right] \ . \tag{3.18}$$

The surface density is $\Sigma_{d,s_i} = M_{s_i}/A$, with A the surface area of the grid cell, so $\Sigma_{d,s_i} = M_{s_i}/[\pi(r_{out}^2 - r_{in}^2)]$ or

$$\Sigma_{d,s_i} = \left(\frac{4\pi}{3}\rho_s\right)^{-\xi} \frac{f_{DG}\Sigma_g}{m_n^{2-\xi} - m_0^{2-\xi}} \left[(\sqrt{s_i \cdot s_{i+1}})^{6-3\xi} - (\sqrt{s_i \cdot s_{i-1}})^{6-3\xi}\right] . \qquad (3.19)$$

Using ξ=11/6 we find

$$\Sigma_{d,s_i} = \left(\frac{4\pi}{3}\rho_s\right)^{-11/6} \frac{f_{DG}\Sigma_g}{m_n^{1/6} - m_0^{1/6}} \left[(s_i \cdot s_{i+1})^{1/4} - (s_i \cdot s_{i-1})^{1/4}\right] . \qquad (3.20)$$

If we use a grain size grid, such as $s_{i+1} = c \cdot s_i$, then the expression can be simplified even more

$$\tilde{\Sigma}_{d,s_i} \propto s_i^{1/2} f_{DG}\Sigma_g . \qquad (3.21)$$

3.2.2   A more complex full grain size distribution

The more advanced step is a grain size distribution that takes into account the coagulation and fragmentation equilibrium as well as erosion of the dust particles in a protoplanetary disc. This was done using the recipe in Birnstiel et al. (2011), where the input parameters are the dust and gas initial surface densities (Σ_d and Σ_g), the local disc temperature (T), the alpha turbulence parameter (α), the volume density of the particles (ρ_s) and finally the fragmentation velocity (u_f), which is the critical velocity above which all collisions lead to either fragmentation or cratering. The logarithmic grid for the sizes is defined as

$$s_{i+1} = 1.12s_i \qquad (3.22)$$

The smallest grain size is 0.025 μm.

Considering that different particle sizes lead to different collision outcomes, this recipe takes into account the relative velocities that particles of different sizes will develop in order to create different regimes for each size. These regimes are created according to size boundaries, within which different power-laws for the fit to the size distribution apply. The smallest particles of the distribution follow Brownian motion, which means their motions are affected by collisions with the gas molecules, there is no preferred direction and they do not have angular momentum. The next regime regards larger particles that start to get affected by turbulent mixing. It was also found (Ormel & Cuzzi, 2007) that when particles have stopping times approximately equal or larger compared to the turn-over time of the smallest eddy of the gas, they start to decouple

The first size boundary can be found by equating the approximate values calculated by Ormel & Cuzzi (2007) with the relative velocity for the smallest grains (Eq. 2.38).

$$s_{BT} \simeq \left[\frac{8\Sigma_g}{\pi\rho_s}Re^{-1/4}\sqrt{\frac{\mu m_p}{3\pi\alpha}}\left(\frac{4\pi}{3}\rho_s\right)^{-1/2}\right]^{2/5} , \qquad (3.23)$$

where the Reynolds number near midplane is

$$Re = \frac{turbulent\ viscosity}{molecular\ viscosity} \simeq \frac{\alpha\Sigma_g\sigma_{H_2}}{2\mu m_p} \tag{3.24}$$

with $\sigma_{H_2} = 2 \times 10^{-15}\ cm^2$ the cross-section of molecular hydrogen, m_p the proton mass and $\mu = 2.3$ is the mean molecular weight in proton masses. Up to this boundary size dust grains are small enough so that they follow Brownian motion in the disc's gas.

The next boundary is at

$$s_{12} = \frac{1}{y_\alpha}\frac{2\Sigma_g}{\pi\rho_s}Re^{-1/2} \tag{3.25}$$

with y_α found to be approximately 1.6 (Ormel & Cuzzi, 2007). This boundary separates between the turbulent regime I and II as described in Section 2.3.

When the Stokes number of a particle becomes larger than the turbulence parameter α then settling starts to become important. We can calculate the corresponding grain size above which settling begins,

$$s_{sett} = \frac{2\alpha\Sigma_g}{\pi\rho_s}\ . \tag{3.26}$$

Finally, we can also estimate the maximum size the grains can reach, since the maximum relative velocity will be $\Delta u \approx \sqrt{\alpha}c_s$ and it must be $\Delta u > u_f$ for a steady-state of grain growth to be established. The maximum size dust particles can reach before they fragment is

$$s_{max} \simeq \frac{2\Sigma_g}{\pi\alpha\rho_s}\frac{u_f^2}{c_s^2}\ . \tag{3.27}$$

Between two boundaries the distribution is described by a power-law $n(m){\cdot}m{\cdot}s = s_i^{\delta_i}$ of different powers δ_i, depending on the regime and whether settling or not occurs within this regime. The powers for each regime are found in Table 3.2 and using these we can create a first fit $f(s_i)$. It is necessary then to include the cut-off effects of the distribution that cause an increase in the fit for large enough particles and a bump caused be cratering. Finally

Regime	Upper end
Brownian motion regime	s_{BT}
Turbulent regime I	s_{12}
Turbulent regime II	s_{max}

Table 3.1: Boundaries for each regime in the grain size distribution, Birnstiel et al. (2011).

Regime	δ_i	
	$s_i \leq s_{sett}$	$s_i \geq s_{sett}$
Brownian motion regime	$\frac{3}{2}$	$\frac{5}{4}$
Turbulent regime I	$\frac{1}{4}$	0
Turbulent regime II	$\frac{1}{2}$	$\frac{1}{4}$

Table 3.2: Power-law exponents for each regime in the grain size distribution (Birnstiel et al., 2011). The distribution in each regime is $n(m) \cdot m \cdot s \propto s_i^{\delta_i}$.

the fit is normalized according to the initial dust surface density at the given location (see Section 5.2 in Birnstiel et al. (2011)).

In Figure 3.3 we can see an example of the grain size distribution. The first region corresponds to the Brownian motion regime followed by very small particles affected by the gas molecules. The upper boundary of this regime is s_{BT} (first vertical line), since the next one regards larger particles that experience turbulent mixing. The boundary s_{12} (third vertical line) divides turbulent mixing in two regimes, since beyond this point, grains are too large and decouple from the gas. The dip after this boundary is caused by a jump in the relative velocities, as for this grain size, the shortest eddy turn-over time is exceeded. An interesting feature in this plot is the bump at the end of the distribution and the increase in the slope, shortly before that. This is an effect due to the cut-off and cratering. The cut-off of the distribution means that near the upper boundary, particles due not have larger particles that they could collide with. Since the model considers a steady-state distribution, the flux needs to be constant, therefore an increase in the number density must be introduced. Cratering is causing a bump and renders the distribution even more top-heavy. The small grains only coagulate, thus creating larger particles, while large grains either get created by the coagulation of the small ones or they collide with fragments and transfer some of their mass, still remaining large particles. To conclude with the boundaries, the second vertical line in Figure 3.3 (s_{sett}) is the boundary above which particles are large enough to be affected by settling. this example, this boundary is within the turbulent regime I, but depending on the gas properties, this boundary can move to other parts of the distribution, within a different regime.

3.2.3   Vertical distribution

The grain size distribution recipes gives the updated dust surface density for a vertically integrated column. In order to calculate the opacities in a 3D code in the radial-vertical
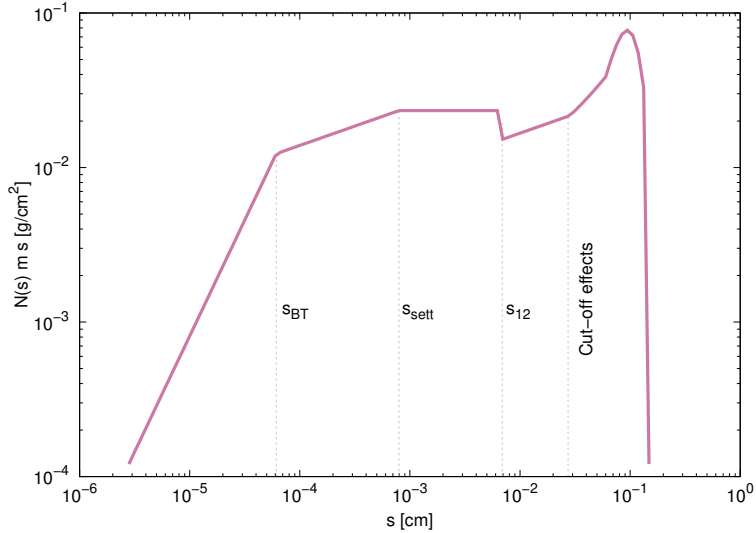
Figure 3.3: Grain size distribution following the recipe from Birnstiel et al. (2011). The surface density contribution of each particle is plotted as a function of the particle's size. The input parameters were: $\alpha = 10^{-4}$, $\Sigma_g = 20$ g/cm^2, $\Sigma_d = 0.2$ g/cm^2, $u_f = 1$ m/s, $T = 50K$, $\rho_s = 1.6$ g/cm^3.

direction as well, we have to first find the midplane volume density (Eq. 2.9). Apart from the vertically integrated surface densities of the grains, Σ_d, which we have from each grain size distribution recipe, we also need the dust scale height. This can be calculated using

$$H_{dust} = H_{gas}\sqrt{\frac{\alpha}{\alpha + St}} \ , \qquad (3.28)$$

so that we also account for the case of $\alpha \gg St$ where we end up with dust coupled to the gas, thus having the same scale height.

Using the midplane dust density we can then assume that the dust is in hydrostatic equilibrium and approximate the volume density in the vertical direction as

$$\rho_d = \rho_{0,mid} \exp\left(-\frac{z^2}{2H_{dust}^2}\right) \ . \qquad (3.29)$$

It should be noted that this equation holds for $z < H_{dust}$.

Eventually, we can use the dust volume density to calculate the average opacity in each grid cell,

$$\bar{\kappa} = \sum_i \frac{\rho_{d,i}}{\rho_g} \times 100 \times \kappa_i \ , \qquad (3.30)$$

with i corresponding to each grain size. In the above expression κ_i are the opacity values as a function of temperature calculated using RADMC-3D. To calculate the opacity, RADMC-3D uses fixed dust-to-gas ratio of 0.01. Therefore, we need to multiply with 100 in order to

get the opacity values corresponding to the dust-to-gas ratio included in the disc. If we only have one grain size and do not consider settling, then ρ_d/ρ_g gives a factor of $1/100$, since it is just the dust-to-gas ratio, and the average opacity is then the corresponding opacity for this grain size κ_i. Equation 3.30 hence automatically includes the effects of settling in the opacity calculation due to the $\rho_{d,i}/\rho_g$ term, that is calculated for each particle in each grid cell.

3.3 Hydrodynamical simulations

The final step is the hydrodynamical simulations using the FARGOCA code (Lega et al., 2014; Bitsch et al., 2014). This is a code that solves the continuity and the Navier-Stokes equations and uses the flux-limited diffusion approach to radiative transfer as described in Section 2.1. The stellar mass is $M_\star = 1 M_\odot$. The inner boundary is at $r_{min} = 1 AU$ and the outer at $r_{max} = 13 AU$. The dust-to-gas ratio is fixed at 0.01. The files produced from RADMC-3D, with the mean Rosseland and Planck opacities as a function of temperature, are read into FARGOCA. These files contain a specified temperature grid, therefore an interpolation is performed to get the correct opacities for each temperature value that can be defined in the hydrodynamical code.

In the simulations performed for this project, the only heating source assumed is the viscous dissipation within the disc that is radiatively diffused and emitted from the disc's surface. However, as it will be discussed in the following paragraph, this heating source is sufficient for the inner part of a disc as in the simulations done for this project. Viscosity in those simulations follows an α prescription (see Chapter 2.1). The gas surface density follows a profile $\Sigma_g = \Sigma_{g,0} \cdot (r/AU)^{-p}$, with $\Sigma_{g,0} = 400 g/cm^2$ and $p = 1/2$ and it does not change during the simulation. For the purposes of this project, viscous heating was assumed to be the only heating source. As the investigation regards the inner parts of the disc, it has been shown that viscous heating is dominating the inner parts (within a few AU) even when stellar heating is taken into consideration (Bitsch et al., 2013). The outer parts get "puffed up" due to the stellar heating caused by the heating of the upper layers by the stellar radiation, but the inner parts are strongly affected by viscous heating and they show no difference with and without stellar heating. The simulations run for some hundreds of orbits (typically 200 orbits) until they reach equilibrium.

At first, I did simulations of single grain sizes in order to see the difference in the disc structures between them. Dust grains affect the hydrodynamical simulation through the opacity in each grid cell. Every simulation has a different grain size and the opacity values for this specific size are used (see Figures 3.1, 3.2). The results of these simulations are presented in the next chapter. The simulations of single sizes offer the chance to examine the extend to which different grain sizes affect the disc's evolution and equilibrium structure and predict how much grain growth or a grain size distribution will change the outcome. The next step is to consider also settling, which was discussed in Chapter (2.3) and how it affects large grains. In this set of simulations each one again had one grain size and the

dust surface density was assumed to be $\Sigma_d = f_{DG}\Sigma_g$ or specifically $\Sigma_d = 0.01\Sigma_g$ as before. This surface density is then translated to a volume density using Equation 3.29 and finally the volume density of dust within a grid cell is used to find the opacity through Equation 3.30, but in this case there is only a single grain size and summing is not needed. But as previously mentioned, the dust-to-gas term for the volume densities includes the settling.

Grain growth that leads to larger dust grains is expected to increase settling and change the disc's structure. Nevertheless, turbulence can counteract settling and lead to the vertical diffusion of particles, which means that several viscosity parameters should be tested in order to understand the effect of settling among different dust sizes. Furthermore, before we can test a full distribution it is crucial to take some smaller steps building up to it, in order to understand in greater depth the results. Additionally, as described at Chapter 3.2.1 a weighting scheme is used, so that opacity is calculated through the dust-to-gas ratio of the volume densities within each grid cell. Therefore we need to test this weighting scheme and make sure any further grain growth test gives reasonable results.

Firstly, I include two grain sizes in the same simulation, 1μm and 1 mm and set the surface density in each grid cell to be a fraction of the total dust surface density, $\Sigma_{d,tot} = f_{DG}\Sigma_g = 0.01\Sigma_g$. Three different test were run for $\Sigma_0 = \Sigma_1 = 0.5\Sigma_{d,tot}$, $\Sigma_0 = 0.25\Sigma_{d,tot}$, $\Sigma_1 = 0.75\Sigma_{d,tot}$ and finally $\Sigma_0 = 0.75\Sigma_{d,tot}$, $\Sigma_1 = 0.25\Sigma_{d,tot}$. It was mentioned in Chapter (3.2) that the mass is expected to be in the large "population" and specifically it has been found that $\Sigma_1 = 0.75\Sigma_{d,tot}$ is a good approximation to the full distribution. Nevertheless, in this first test all of the aforementioned fractions have been used to test the weighting scheme and compare their results. In the next test, more grain sizes were included, at first 5 different grain sizes in the same simulation and then 10. The surface densities were this time $\Sigma_0 = 0.25\Sigma_{d,tot}$, $\Sigma_1 = 0.75\Sigma_{d,tot}$ for the small and the large population correspondingly. As a first step, the grains were divided into the two populations by a fixed grain size. Particles up to $s_{sep} = 10\mu m$ belong in the small population and those above this size belong to the large population. This is a rather arbitrarily chosen separation size for the two populations, I have also tested a boundary that depends on the disc properties to test.

Finally, we can also change the number of grain sizes considered. Instead of having a specified number of grain sizes (2, 5 or 10 for example) we can create a logarithmic grid of sizes as in Birnstiel et al. (2011) ($s_{i+1} = 1.12s_i$). This way each population has a finer resolution, but the impact on the resulting disc structure is not expected to change significantly especially for the models with fixed surface densities in each population. Using RADMC-3D (see Chapter 3.1) a number of files is created with opacity values as a function of temperature. These files are then used in the hydrodynamical code (FARGOCA). The opacity calculations from these files are then interpolated and in this way each grain size that is included in the simulations gets an opacity value in each grid cell. The reason that the interpolation is done instead of directly calculating opacity using Mie theory is because of the computational time, which would be very long. If the number of grain sizes used is less or equal to the number of opacity files available, then each grain size gets its corresponding opacity values calculated through Mie theory from RADMC-3D. If the

number of grain sizes is greater than the number of files available then the needed opacity grid is filled in by the interpolation.

After those tests that will help understanding the implementation of models with full distributions, the next step is to try the models described in the previous section (Ch. 3.2). In the first model to be simulated, the surface densities of the grains are calculated by Equation 3.20. The next simulation is the more complex distribution from Birnstiel et al. (2011) that includes coagulation, fragmentation and cratering (Ch. 3.2.2). The grains included in the aforementioned models can be chosen to be either of 10 different sizes or of sizes defined by a grid so that the resolution is increased. The upper boundary is fixed for the Dohnanyi (1969); Tanaka et al. (1996) model and defined by the fragmentation barrier in Birnstiel et al. (2011).

The results from the simulations discussed in this section are presented in the next Chapter and the tables for the corresponding simulations can be found in Appendix B. Most of the results will be presented through plots of the aspect ratio as a function of orbital distance, since such plots contain most of the necessary information to understand the disc structure. First of all, the aspect ratio is connected, by hydrostatic equilibrium, to the midplane temperature, $T_{mid} \propto (H/r)^2$ (Equation 2.13). Therefore the aspect ratio as a function of orbital distance gives indications for the thermal structure of each disc. Additionally, these plots show the location of the iceline which is more difficult to distinguish in a plot of the temperature as a function of orbital distance and height (see Figure 4.1 and 4.2). Apart from the direct information, we can also get direct indications for the implications of the results. For example, it is possible to discuss planetesimal formation or planet migration, in a protoplanetary disc as the ones simulated here, using the aspect ratio and its radial gradient. Such implication will be discussed in Chapter 5.

Chapter 4

Results

4.1   Single grain sizes

The first part of this project involves simulations of discs with single grain sizes, where all particles within one simulation have the same size. It should be noted that dust particles are not actually included in the simulation, but their effect is incorporated through the opacity that they provide to each grid cell. I initially tested five different grain sizes from 0.1 μm to 1 mm (Runs 1-5, Table B.1) and the resulting aspect ratio of the protoplanetary disc is plotted as a function of radius in Figure 4.1. Each simulation has only one specific grain size with a surface density of $\Sigma_d = f_{DG}\Sigma_g$. The dust-to-gas ratio f_{DG} is 1% in all of the simulations.

The first set of simulations was done using a high alpha parameter, namely $\alpha = 10^{-2}$ and the runs reached equilibrium after 200 orbits. In Figure 4.1 we can see the aspect ratio (H/r) as a function of orbital distance from the star for simulations of different grain sizes. We firstly discuss the simulation with 0.1μm, which roughly corresponds to an unevolved dust population as found in the interstellar medium. The simulation with particles of 0.1μm (dark blue line) results in an increasing aspect ratio as a function of orbital distance up to 3 AU, where it reaches a maximum and then decreases up to the outer disc boundary at 13 AU. Using 1μm-sized particles (light blue line) we see a similar disc structure. The aspect ratio is almost constant for the first few AU and has a small increase at 3 AU. Then it converges with the simulation of 0.1μm. If the grain size increases to 10μm (pink line), then the aspect ratio also increases with distance, features a bump closer to 4 AU and decreases with the same slope as the previous two simulations. The larger particles have distinct profiles. Specifically, the aspect ratio of the simulation with particles of 0.1 mm (orange line) is a monotonically increasing function of orbital distance with a small bump at 2 AU. The same can be seen for the simulation with the largest particles, namely 1 mm (red line), but in this case a bump is not visible at any parts of the aspect ratio profile.

The bump that is observed in several of the aforementioned aspect ratio profiles cor-

responds to the iceline, the location prior to which water-ice sublimates. The connection between opacity and temperature is illustrated in Figure 3.1 and since temperature is proportional to the aspect ratio we can follow the same figure to understand the results. There you can see that the iceline is a sharp bump in the opacity profiles of the smaller particles of the set, while it causes a decrease in the opacity of the largest particles. The mixture used in the simulations is 50% water-ice and 50% silicates. Therefore this decrease in the opacity interior the iceline is due to the loss of water-ice. After this point, the opacity is only determined by the silicates.
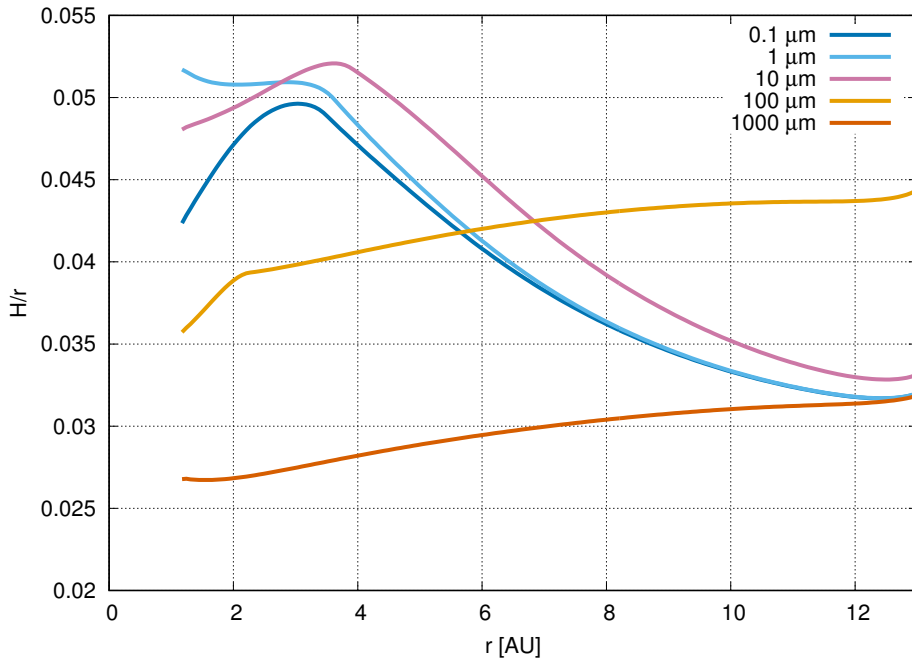

Figure 4.1: Aspect ratio as a function of orbital distance in AU, for discs with 5 different grain sizes from 0.1 μm to 1 mm. All of the simulations include only viscous heating and have $\alpha = 10^{-2}$ as the turbulence parameter in viscosity. Settling is not considered in this set of simulations. The disc model with 0.1 μm-sized grains is plotted in dark blue and has a very prominent iceline bump at 3 AU, while beyond the iceline, as the orbital distance increases and the temperature drops, the aspect ratio also decreases. The model with 1 μm in light blue has almost the same aspect ratio, except for the region interior to the iceline which, as we can see in Figure 3.1, has higher opacity. The pink line corresponds to the disc with 10 μm-sized dust particles and in this case the iceline has slightly moved outwards, in contrast to the 0.1 mm disc in orange where the inner disc is much colder and the iceline has moved closer to the star. The coldest disc is the one with 1 mm-sized particles, in which the iceline bump in the aspect ratio is barely seen at the inner boundary of the simulations. The general trend is that as grain size increases, the disc becomes colder, leading to a lower aspect ratio and the iceline moves inwards.
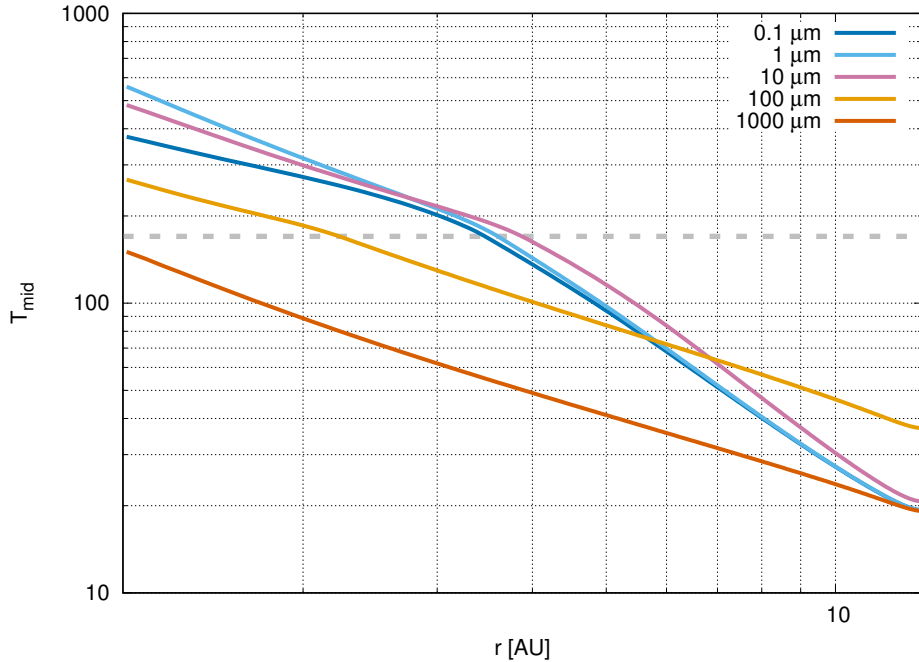
Figure 4.2: Temperature as a function of orbital distance for the same simulations that are presented and discussed in Figure 4.1. A horizontal dotted gray line at 170 K is overplotted and we can see a change in the slope around it, but the iceline is otherwise indistinct in this plot. On the other hand, the iceline is evident in the aspect ratio as a function of orbital distance (Figure 4.1).

The aspect ratio is a decreasing function of orbital distance for small particles and increasing for the largest particles because of the mean Rosseland opacity that has also an indirect dependence on the disc's radius due to the change in temperature of the disc with orbital distance. As the orbital distance increases, temperature decreases and the opacity gets lower for small particles, while it is independent of radius for large particles (greater than 0.1 mm). Another important note from Figure 4.1 is the pattern beyond approximately 7 AU. Even though prior to that, the aspect ratio decreases if the grain size increases, after this point, the disc profile where 0.1 mm are present, is higher compared to those of the smaller particles. This happens because opacity at a hundred Kelvin or less is higher for the 0.1 mm-sized grains. A more detailed explanation to why this is the case was discussed in Chapter 3.1.

It is interesting that the disc with the largest grains features no bump. This disc has such a low aspect ratio and as a consequence is so cold that the iceline is not present, within the chosen inner boundary of our simulations. Both of the profiles for the two largest sizes, 0.1 and 1 mm are almost flat, which is also expected since opacity as a function of temperature for those is almost constant (see Figure 3.1). Therefore, the general trend is that the larger the grain size, the colder the disc becomes with lower aspect ratio and the iceline moves inwards. Nevertheless, the 10 μ and 0.1 mm discs make some exceptions to

this description, as in the former the iceline bump is further away compared to discs with smaller particles and in the latter the aspect ratio (or the temperature) is the highest after approximately 7 AU.

The midplane temperature as a function of orbital distance is plotted in Figure 4.2. The horizontal dotted gray line denotes the T=170 K, the temperature around which we find the iceline transition. The midplane temperature is connected to the aspect ratio (Figure 4.1) by the hydrostatic equilibrium (Equation 2.13). However, as it was discussed in the final paragraph of Chapter 3.3, the aspect ratio as a function of orbital distance offers more information related to the disc structure. One important feature is the iceline, which is evident as a bump in the plot of aspect ratio as a function of orbital distance. On the contrary, the change of slope in the temperature as a function of orbital distance is indistinct and makes the location of the iceline less obvious.

The opacity and temperature within the disc for 1 μm and 1 mm is plotted in Figures 4.3a to 4.3d as a function of orbital distance on the x-axis and height on the y-axis. The highest opacity values in the 1 μm figure or the bump in the aspect ratio profile) correspond to the iceline as it can be also seen in the temperature figure, where the iceline zone is marked with a brighter yellow. In this plot (Figure 4.3a) it is easier to see the transition of the opacity slope around the iceline due to the water-ice loss, from positive to negative. The corresponding figures for 1 mm are both uniform since, as it was mentioned, opacity is constant with temperature for these grains except for the iceline transition which is not present in these simulations. In the opacity plots the $\tau = 1$ line is overplotted in red (it should be noted that the steps that this line shows are numerical artefacts). The optical depth τ is defined as

$$\tau = \int_z^0 \kappa_R \rho_g dz \ , \tag{4.1}$$

therefore it increases as the height z is decreasing. When $\tau \geq 1$, then the disc is optically thick or in other words, the mean free path of the photons is much smaller than the length scale over which temperature changes.

The $\tau = 1$ line marks the difference between optically thick and thin medium. In optically thin parts of the disc, photons can "freely" travel out of the disc. The $\tau = 1$ line thus marks the region of the disc where cooling becomes efficient. A $\tau = 1$ line close to midplane corresponds to lower opacities (if the density stays constant), which results in a cooler disc. In the case of millimetre-sized particles, dominating the opacity, we see that the $\tau = 1$ line is closer to midplane, hence resulting in a strong cooling and colder disc (as is evident in Figure 4.3a).

4.1.1   Dependence on α-viscosity

Three different sets of simulations were performed, for $\alpha = 10^{-2}$, 10^{-3} and 10^{-4}, in order to test the influence of viscosity. The decrease in this parameter causes a decrease in the viscous heating and since temperature is connected to the aspect ratio through the hydro-
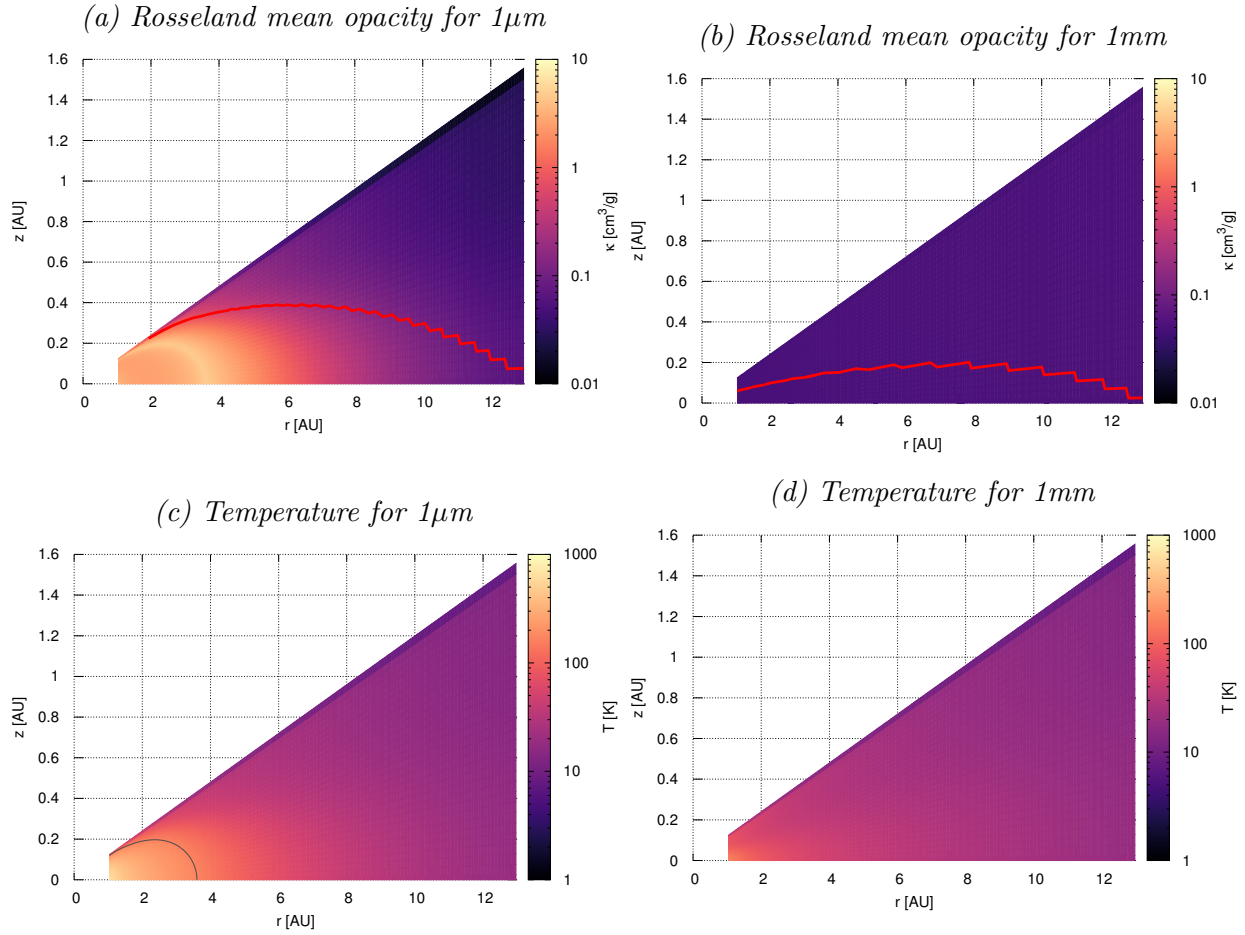
Figure 4.3: Protoplanetary disc simulation of 1 µm (top) and 1 mm (bottom), for $\alpha = 10^{-2}$. In the top left plot (a) we show the Rosseland mean opacity for 1µm, while in the bottom left we show the temperature for the same grain size, both as a function of orbital distance and height. There is a distinct ring that has the highest opacity values in Figure (a) which corresponds to the iceline as we can see in Figure (c), where the iceline region is overplotted in gray. The 1 mm opacity plot is almost uniform as expected and so is the temperature plot as the temperature is around 20 K in most parts of the disc. The red line in the opacity plots is the optical length $\tau = 1$.

static equilibrium (Equation 2.13) it is expected that the aspect ratio will also decrease. The choice of low α-parameters is motivated by recent studies that argue viscosities may be low in protoplanetary discs, where angular momentum is dominantly transported by disc winds (Bai & Stone, 2013; Gressel et al., 2015; Bai, 2017; Suzuki et al., 2017).

If we use $\alpha = 10^{-3}$ (Runs 6-10, Table B.1) then, as we see in the left plot in Figure 4.4, the discs featuring all the various grain sizes become a lot colder and the simulation of the 0.1 mm-sized dust particles leads to the highest aspect ratio profile already outside of 2 AU.

Additionally, the simulation of the 1 mm-sized particles also leads to higher aspect ratio profile compared to those of the smaller particles at around 4 AU. It is also interesting that all of the aspect ratio profiles, apart from the 0.1 mm, are almost the same and constant in radius. In summary, when turbulence decreases, viscosity is less effective at heating which leads to colder discs. Then the differences in disc structure between grain sizes in the 1-13 AU region of the disc become similar. The iceline bumps are only slightly visible near the inner boundaries for the 0.1-10 μm simulations and they are absent for the other two simulations with large particle size. Again in this case, the 1 mm disc is colder near midplane.
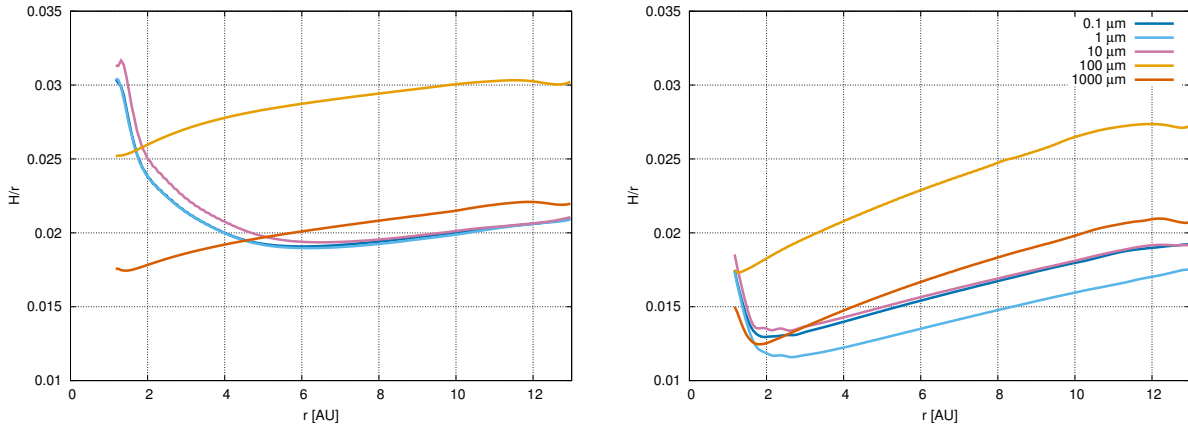

Figure 4.4: Aspect ratio as a function of orbital distance for protoplanetary disc simulations of single sizes (0.1 μm-1 mm). In the left plot the simulations were run for $\alpha = 10^{-3}$ and in the right for $\alpha = 10^{-4}$. Lower turbulence leads to progressively colder discs and almost independence from particle size. The 0.1 mm-sized grains have higher opacities in low temperatures and that distinguishes the resulting disc structure (orange line) from other grain sizes, since temperature and aspect ratio get higher.

The final set of simulations has $\alpha = 10^{-4}$ (Runs 10-15, Table B.1). With less turbulence, viscous heating decreases even further and the discs become once more even colder resulting in lower aspect ratios. Both of the simulations with the largest grain sizes, 0.1 and 1 mm, now have higher aspect ratios compared to the simulations with smaller particles outside of approximately 3 AU. In general, this behaviour can be explained by the fact that opacity is constant for those large particles in most temperature regions relative to the simulations in this project. Even though opacity is around two orders of magnitude higher for small particles (Figure 3.1), it gets almost one order of magnitude lower if temperature drops below 20-30 Kelvin.

To summarize section 4.1, which does not include the effect of settling, we find that the small grains result in similar aspect ratios, while the larger ones have significantly lower values for $\alpha = 10^{-2}$. This changes progressively as we go to lower α values or lower turbulence and correspondingly less efficient viscous heating. Especially at temperatures of a few Kelvin, the disc structure is nearly independent of grain size if we consider dust

particles to be less than 10 μm. Larger sizes lead to differentiation in the structure, it increases the opacity of the disc and gives higher aspect ratio due to the low temperature where the opacity is higher for larger grains. We can also see that the location of the iceline also moves closer to the star with decreasing α-viscosity. It should be finally noted that the Bell & Lin opacity law (1994) which is used widely in disc simulations, employs ISM-sized grains and results in discs with similar aspect ratio as the smaller grains that are presented here. This implies that if the larger grains are more abundant in protoplanetary discs, then the resulting discs will deviate strongly from what has been expected.

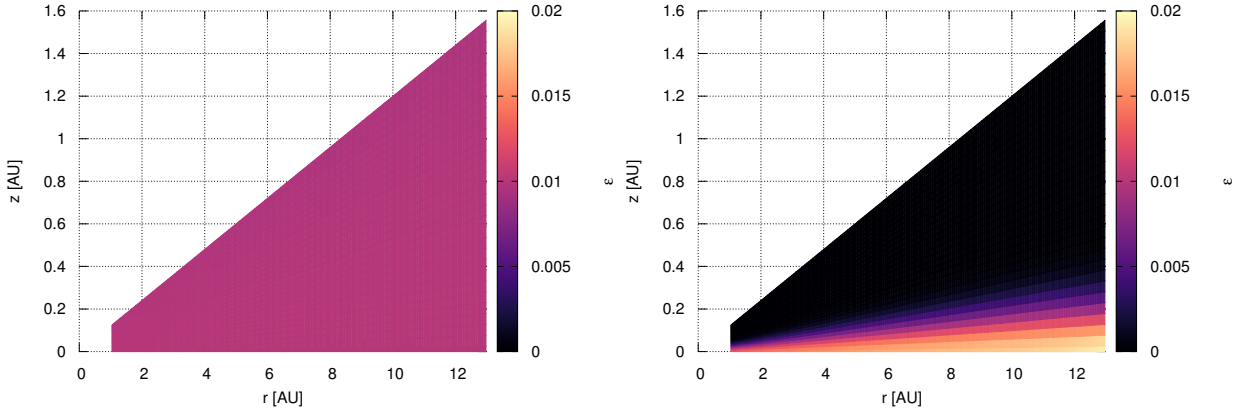## 4.2 Single grain sizes including settling

Figure 4.5: Dust-to-gas density, micrometre-sized dust on the left and millimetre-sized on the right, $\alpha = 10^{-3}$, with settling. The simulation of 1 μm-sized dust grains shows no settling and therefore the dust-to-gas ratio remains fixed at 1%. On the other hand, settling affects the 1 mm-sized particles, so that the dust-to-gas ratio in the upper layers of the disc becomes almost zero.
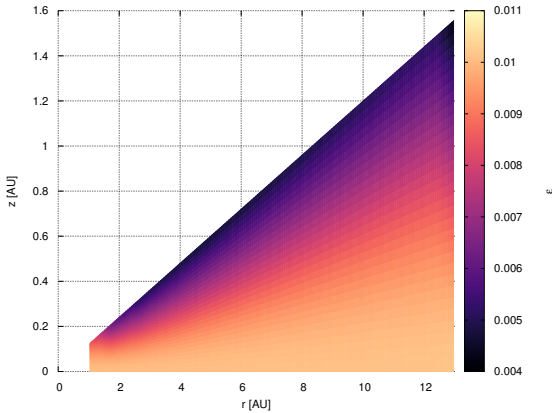

Figure 4.6: Dust-to-gas density, micrometre-sized dust, $\alpha = 10^{-4}$, with settling. With sufficiently low α values, settling starts to affect even the smaller particle sizes considered here.

The turbulence in a disc's gas causes the dust particles to be vertically diffused. Turbulent stirring is counteracted by gravity for grains that become more decoupled from the gas. This is illustrated in Figure 4.5, where we see in the left plot that the dust-to-gas ratio is uniform for small particle sizes, but it is almost zero at the upper layers for larger particles and most of the dust mass is now concentrated at midplane (right plot).

The aspect ratio or the dust scale height depends on the α parameter and the Stokes number of the dust particle (see Equations 2.49 and 2.61). Consequently, when the

turbulence parameter changes, so does the dust scale height, since less turbulence means more settling and less particles in higher heights of the protoplanetary disc. We do not expect particle settling to affect the models with $\alpha = 10^{-2}$. Indeed, the same simulations of 5 different grain sizes were performed including the effect of settling and no difference in the disc structure was found compared to the simulations without settling (Runs 16-20, Table B.1). On the contrary, in Figure 4.7 we can see that low α simulations (Runs 21-30, Table B.1) show an effect on the disc structure, especially for larger particles. With $\alpha = 10^{-3}$ the effect starts on the 10μm disc, whereas for $\alpha = 10^{-4}$ even the 1μm simulation gets affected (Figure 4.6).

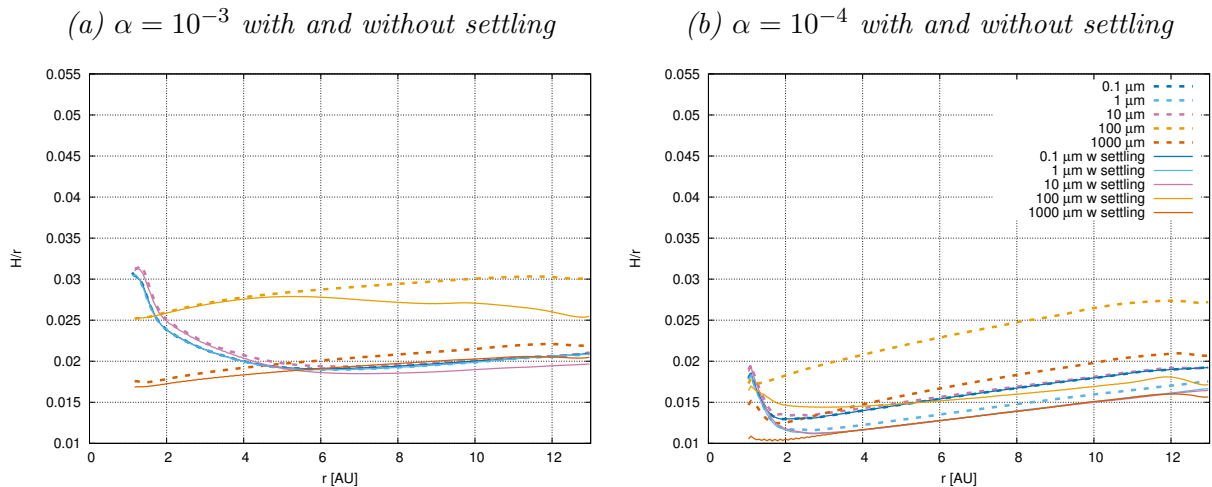*Figure 4.7: Aspect ratio as a function of orbital distance for protoplanetary disc simulations of single sizes (0.1 μm-1 mm) with settling. In the left plot the simulations were run for $\alpha = 10^{-3}$ and in the right for $\alpha = 10^{-4}$. Due to settling, the opacity in the midplane decreases, thus the cooling rate increases and the disc becomes colder with lower aspect ratio. With $\alpha = 10^{-3}$ the 0.1 mm-sized grains (red line) and 1 mm (orange line) are affected by settling, while with lower α settling affects also the 10 μm (pink line) and even 1 μm (light blue line). The dashed lines show the aspect ratios without settling for comparison.*

A very important observation in Figure 4.7 is the fact that with settling all of the simulations are almost independent of dust grain size, especially at larger orbital distances. The main exception is the 0.1 mm particles with $\alpha = 10^{-3}$. The temperature in the simulation with the 0.1 mm particles is below 50 K, where opacity is still independent from temperature for the 0.1 mm grains, but higher compared to the opacity of smaller particles and the millimetre-sized. The decrease in the aspect ratio compared to the previous case of $\alpha = 10^{-2}$ is in this case, connected to the decrease in the α parameter itself and not on a drop in opacity. With $\alpha = 10^{-4}$ the temperature gets even lower so the disc with 0.1 mm particles now depends on temperature, too. Thus, the corresponding opacity drops
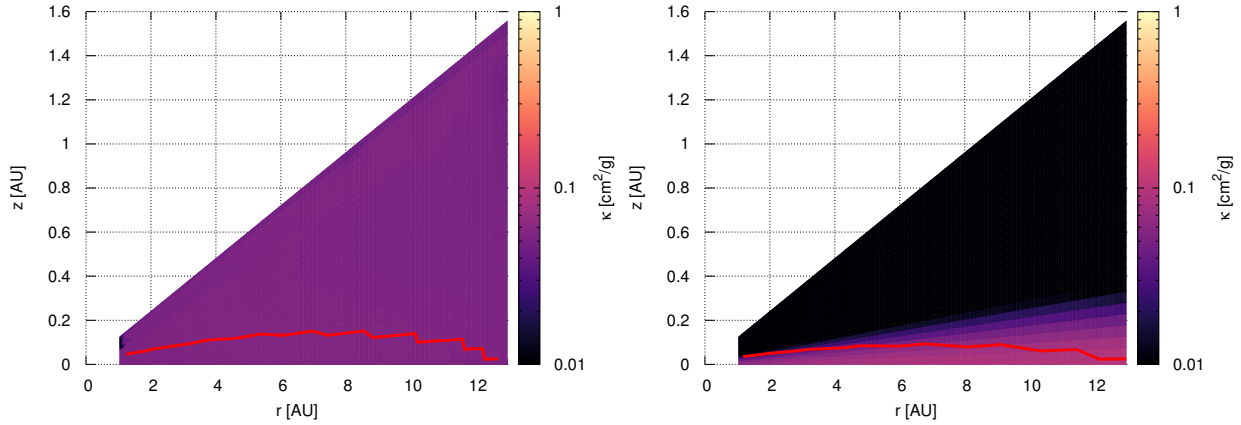
significantly (Figure 4.8).

Figure 4.8: Mean Rosseland opacity, micrometre-sized dust, without settling on the left and with settling on the right, $\alpha = 10^{-3}$. The red line denotes the optical depth $\tau = 1$. The optical depth increases as height decreases and the disc gets optically thick. Since the disc is very cold, the simulation of the 1 mm-sized particles has, once more, low, almost constant opacity values.

4.3   Grain size distribution

The final set of simulations involves a path towards understanding the influence of grain growth on the structure of protoplanetary discs. The effect of settling is automatically added to the models as the volume density dust-to-gas ratio of each particle is used in order to calculate the effective opacity in each grid cell (see Chapter 3.2.2 and Equation 3.30).

4.3.1   Multiple grain sizes in discs

The simulations that were presented in the previous sections, all included single grain sizes with surface densities related to the gas surface density through the dust-to-gas ratio. In this part of the project the goal is at first to include the effect of more grain sizes within the same simulation. To begin with, as a test to the weighting that has been implemented in the code, I have included two grain sizes, namely 1 μm and 1 mm and done three separate simulation varying the surface density of each dust grain size (Runs 31-33, Table B.2). Specifically, the first simulation had $\Sigma_0 = \Sigma_1 = 0.5\Sigma_{d,tot}$, where Σ_0 is the surface density of the smaller particle (1μm), Σ_1 is the surface density of the larger particle (1 mm) and $\Sigma_{d,tot} = f_{DG}\Sigma_g$, thus keeping the total dust surface density equal to 1% of the gas surface density. The second simulation had $\Sigma_0 = 0.25\Sigma_{d,tot}$ and $\Sigma_1 = 0.75\Sigma_{d,tot}$ and finally the third simulation featured $\Sigma_0 = 0.75\Sigma_{d,tot}$ and $\Sigma_1 = 0.25\Sigma_{d,tot}$. Those three simulations

are presented in Figure 4.9a, where the single size simulations using 1, 100 and 1000 μm particles are also plotted for comparison. This test ensures that the opacity weighting is done correctly and we find that the aspect ratio changes according to the given surface densities ratio between the small and the large particles.

4.3.2 Test on the number of particle size bins used

Additionally, I have increased the number of grain sizes used in each model and ran two more simulations with 5 and 10 different grain sizes (Runs 34-35, Table B.2). The model with 5 grain sizes includes the 5 sizes used in the first sets of simulations (Chapters 4.1 and 4.2) from 0.1 to 1000 μm, whereas in the model with 10 grain sizes the range is from 0.03 to 1000μm and it includes the geometric means between each size in the 5 grains model. So, starting from 0.03μm we then have 0.1, 0.3, 1, 3, ..., 1000μm sized grains. The aspect ratios for the resulting disc in equilibrium are presented in Figure 4.9b and we can see that since the various grain sizes have different opacities, changing the number of sizes considered will change the disc's structure. However, including more and more sizes eventually results in convergence.

(a) Models with 2 grain sizes of 1μm and 1mm, with different surface density fractions.
(b) Models with 2, 5 and 10 grain sizes between 0.03μm and 1mm.
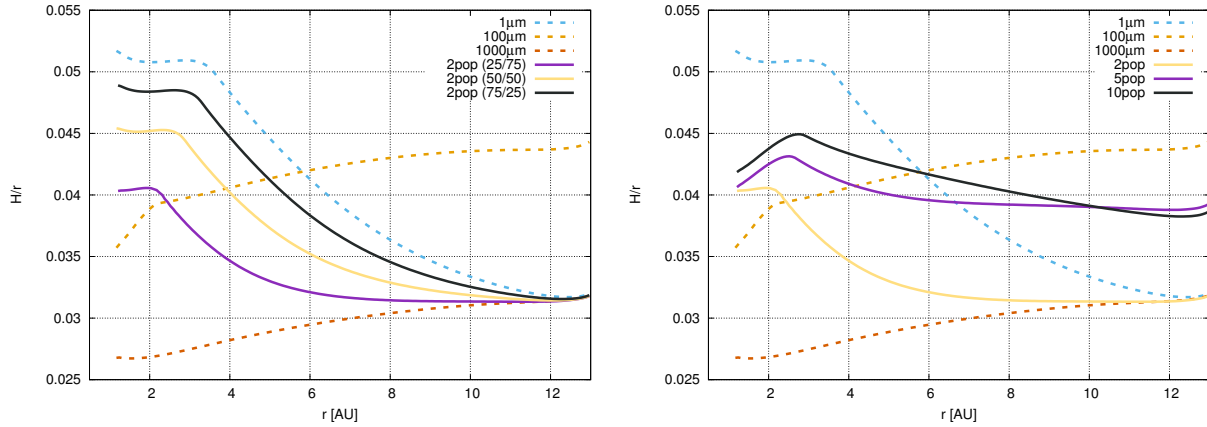

Figure 4.9: In the left plot we have three models, all with 2 grain sizes of 1 μm and 1 mm. In the first case the surface densities were equal, while in the second the small particles have $25\% \cdot \Sigma_{d,tot}$ and the large have $75\% \cdot \Sigma_{d,tot}$. Finally, in the third model the small particles have $75\% \cdot \Sigma_{d,tot}$ and the large $25\% \cdot \Sigma_{d,tot}$. In the right plot, we have three models with 2, 5 and 10 different sizes, where the small particles have $25\% \cdot \Sigma_{d,tot}$ and the large have $75\% \cdot \Sigma_{d,tot}$. The size that separates these two populations is fixed at 10μm.
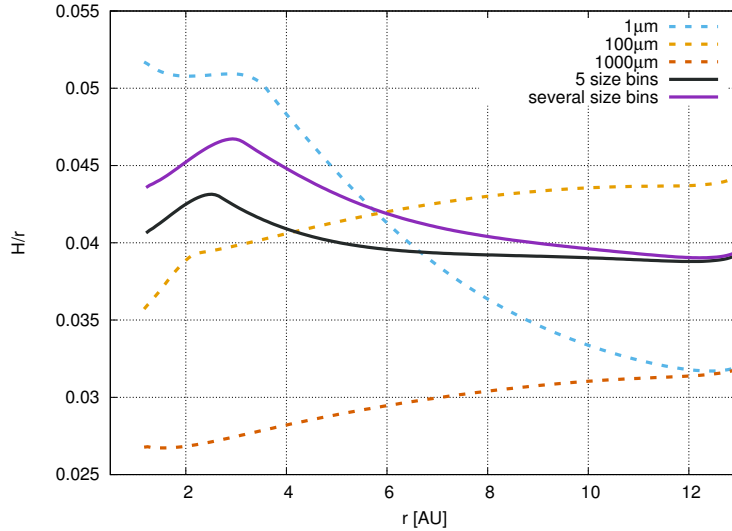
Figure 4.10: In both models the small particles have $25\% \cdot \Sigma_{d,tot}$ and the large have $75\% \cdot \Sigma_{d,tot}$ with a separation size $s_{sep} = 10\mu m$. In the first case (black line) the simulation includes 5 different sizes, whereas in the second (purple line) a size grid has been implemented.

4.3.3 Test on opacity file interpolation

It should be noted here, that when the number of opacity files is greater or equal to the number of grain sizes used, then each grain size gets its exact opacity values accordingly. On the other hand, if the number of opacity files is smaller compared to the grain sizes used, then some of the grains will get opacity values according to the interpolation of the values in the existing files. An interpolation is needed because the computational time to calculate the opacity for each grid cell using Mie theory (as in RADMC-3D) would be too long. Therefore, we need to choose a specific number of files and interpolate between them to get a complete grid of opacity calculations as a function of temperature. The opacity values that are calculated through the interpolation might have a small deviation from the exact value calculated using Mie theory. This has been tested using 10 grain sizes and running two simulations, with 5 opacity files in the first case and 10 opacity files in the second case (Runs 35-36, Table B.2). A small difference has been found between them (see Figure 4.11b) and even though it is not enough to significantly alter the results, in the following simulations 10 opacity files have been used.

4.3.4 Full particle size distributions

Afterwards, instead of employing an arbitrary surface density for each grain, we can use the distribution described in Chapter 3.2.1 and resulting in Equation 3.20. This model (Run 38, Table B.2) takes into account fragmentation due to collisional cascade. The slope for the mass or surface density of the grains follows $n(m)dm \propto m^{-11/6}dm$ (Dohnanyi,

(a) Mean Rosseland opacity as a function of tem- *(b) Test on the number of the opacity files and*
perature   *the interpolation performed*
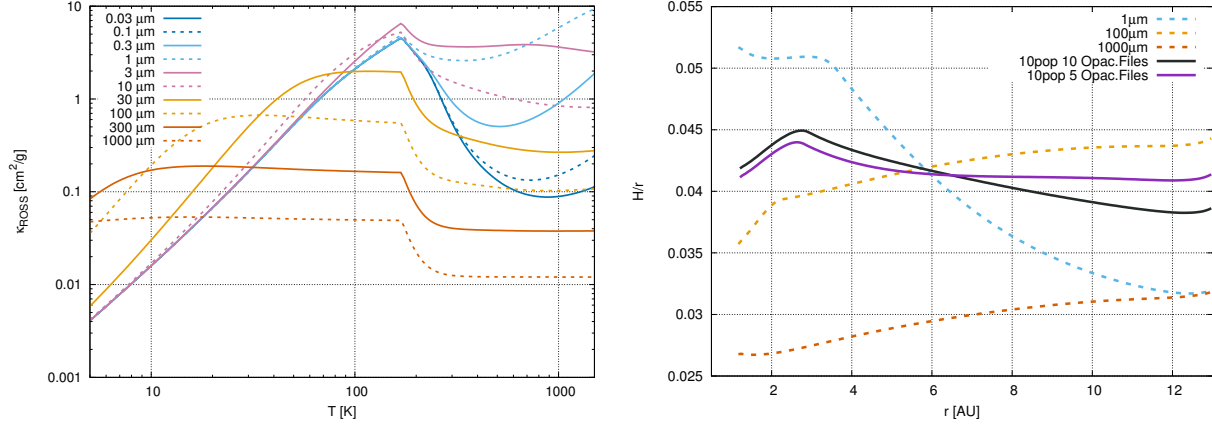

Figure 4.11: *In the left plot we illustrate the mean Rosseland opacity as a function of temperature for 10 grain sizes from 0.03 to 1000 μm. In the right, the test regarding the opacity interpolation is presented. Specifically, 10 size bins where tested with 5 and 10 opacity files. The surface densities in this test are* $25\% \cdot \Sigma_{d,tot}$ *for the small particles (¡ 10 μm) and* $75\% \cdot \Sigma_{d,tot}$ *for the large.*

1969; Tanaka et al., 1996). Translating the mass distribution into surface densities we find $\Sigma_{d,s_i} \propto s_i^{1/2} \Sigma_{d,tot}$. The lower grain size considered is 0.03 μm and the greatest is 1000μm, while the grain size grid is defined as $s_{i+i} = 1.12 s_i$. The number of opacity files used is 10 and an interpolation is done to define the opacity in all of the size bins used.

In Figure 4.12 we can see the aspect ratio of the disc that includes this grain size distribution (purple line). The aspect ratio profiles of 1 μm (light blue dashed line), 0.1 mm (red dashed line) and 1 mm (orange dashed line) have been also plotted for comparison. In the full grain size distribution simulation, the iceline, which causes the bump at 2.5 AU, has moved inwards compared to the simulations of small single particles (0.1 to 10 μm) since this disc is colder. As a total, the aspect ratio is almost constant, but the distribution is strongly influenced by the particles around 0.1 mm, because the rest of the simulations for smaller particles result in discs with lower aspect ratio near the outer boundaries. The opacity for the 0.1 mm particles at the outer parts of the disc is independent of temperature. In contrast to the single size model of 0.1 mm, inner to 4 AU the disc is hotter. The slope used for the mass distribution indicates that small particles contribute less to the mass and consequently density and opacity. Therefore at the inner disc, the grain size distribution simulation has higher aspect ratio compared to the 0.1 mm, but it is significantly lower than the profiles of the smaller particles.

Finally, the grain size distribution from Birnstiel et al. (2011) is presented (Run 39, Table B.2). It is illustrated in Figure 4.13 (black line), along with the previous model of
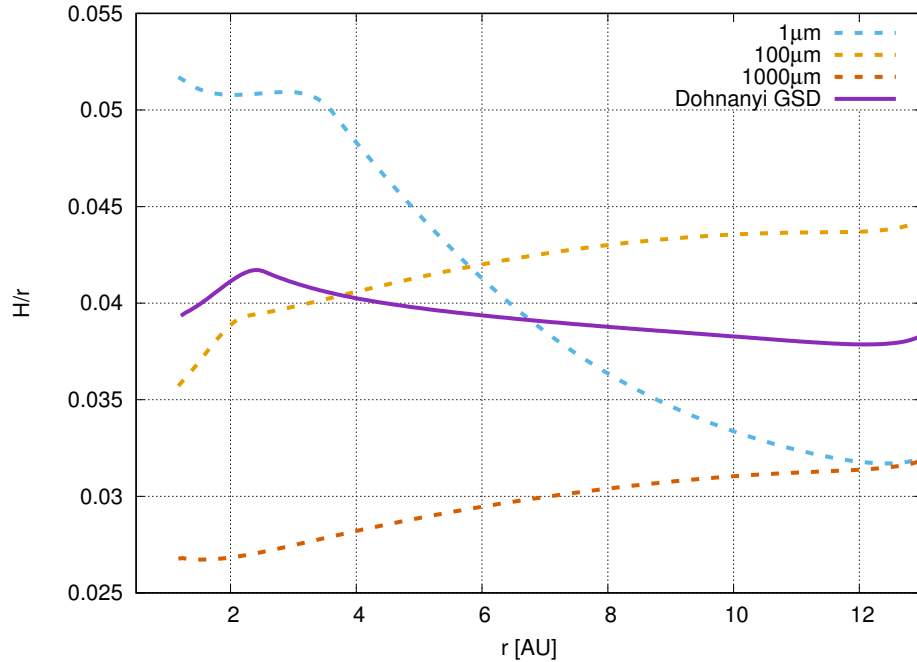
Figure 4.12: Full grain size distribution where the surface densities are defined as a slope, following a mass distribution of $n(m)dm \propto m^{-11/6}dm$ (Dohnanyi, 1969; Tanaka et al., 1996). The dust surface density in this case is $\Sigma_d \propto s^{1/2}\Sigma_{d,tot}$. The grain sizes that are included range from 0.03 to 1000 µm In comparison the single grain size simulations for 1, 100 and 1000 µm-sized particles are included in the light blue, red and orange dashed line. The viscosity parameter is $\alpha = 10^{-2}$. The size distribution leads to an almost flat aspect ratio. The aspect ratio profile falls mostly between the two larger particles, 0.1 and 1 mm, apart from the region inner to 4 AU which is hotter, due to the contribution from the smaller particles with larger opacities.

Dohnanyi (1969); Tanaka et al. (1996), for comparison (purple dashed line). In this case, the single size simulations plotted for reference are for the 3 µm (light blue dashed line), the 10 µm (pink dashed line), the 30 µm (red dashed line) and the 1 mm as before (orange dashed line). The Birnstiel et al. (2011) model includes coagulation and fragmentation as well as partial loss of mass due to collisions (cratering). The mass distribution initially is considered to be the same as in the previous model, so $n(m)dm \propto m^{-\alpha}dm$, but this time the grain sizes are divided into different regimes depending on their relative velocities within the disc (see Chapter 3.2.2). Each regime then, starting with $n(m)dm \propto m^{-\alpha}dm$, gets a different slope adapted accordingly. The grain size distribution is different in each grid cell, since it depends on the temperature of the disc and the total dust and gas surface densities which have radial dependence. It then gives the vertically integrated surface density for each particle and using that we can calculate its contribution to the opacity at each grid cell (see Equation 3.30). As the opacity changes, so does the temperature of the disc since the cooling rate is affected. Therefore we have a feedback loop where the

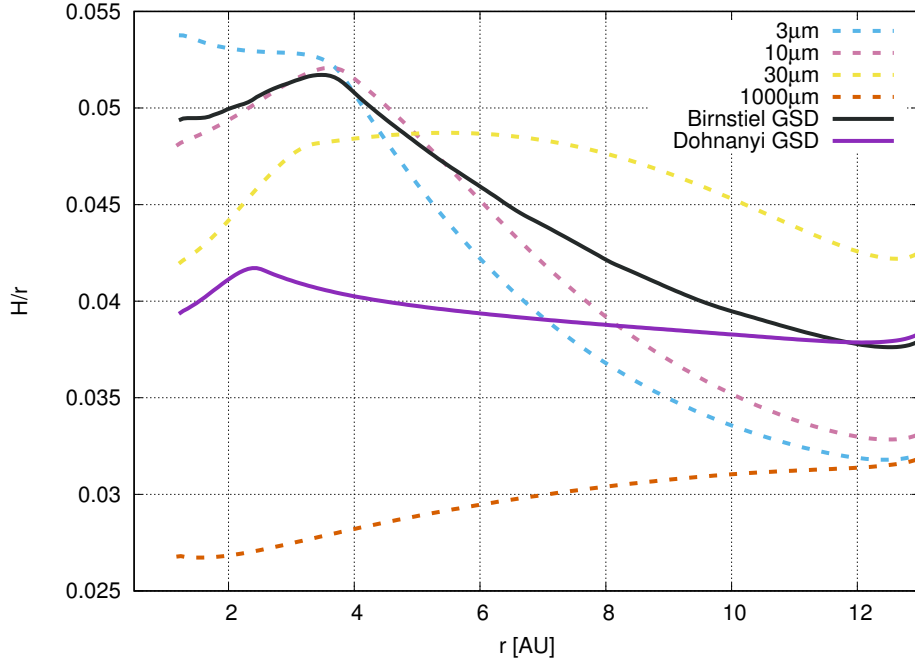temperature changes and then so does the grain size distribution.

Figure 4.13: Model from Birnstiel et al. (2011) (black line). The Dohnanyi (1969); Tanaka et al. (1996) model is plotted for reference (purple line and the single size distributions for 3, 10, 30 and 1000 μm (light blue, pink, red and orange dashed line). The two models converge at the outer boundary of 13 AU and deviate at the inner boundary (1 AU). The difference is caused by the upper boundary of the size distribution, where the Dohnanyi (1969); Tanaka et al. (1996) distribution allows large particles with lower opacities compared to the Birnstiel et al. (2011) simulation.

The two grain size distribution models have similar aspect ratio profiles near the outer boundary of 13 AU. As explained in the previous sections, closer to the outer boundaries the aspect ratio is almost independent of grain size. The profile near the outer boundary is affected again by the 0.1 mm and this time also by the 30 μm sized particles. Near the inner boundary of the disc, the difference between the two models can be explained because of the different upper boundary in grain size. In the first model (Figure 4.12), the upper boundary is fixed at 1 mm. On the other hand, in the second model discussed here (Figure 4.13) the upper boundary is determined by the maximum velocity that particles can reach before fragmenting. This means that in each part of the disc the relative velocities of the particles are different and the maximum possible grain size is changing. In total, the upper boundary in this model is defined by smaller particles compared to the previous case (see Figure 4.14 and 4.15), especially near the inner edge where the temperature is higher and the fragmentation barrier lower (see also Figure 2.2). These small particles lead to a large opacity, hence temperature and thus larger aspect ratio compared to the Dohnanyi (1969); Tanaka et al. (1996) distribution.
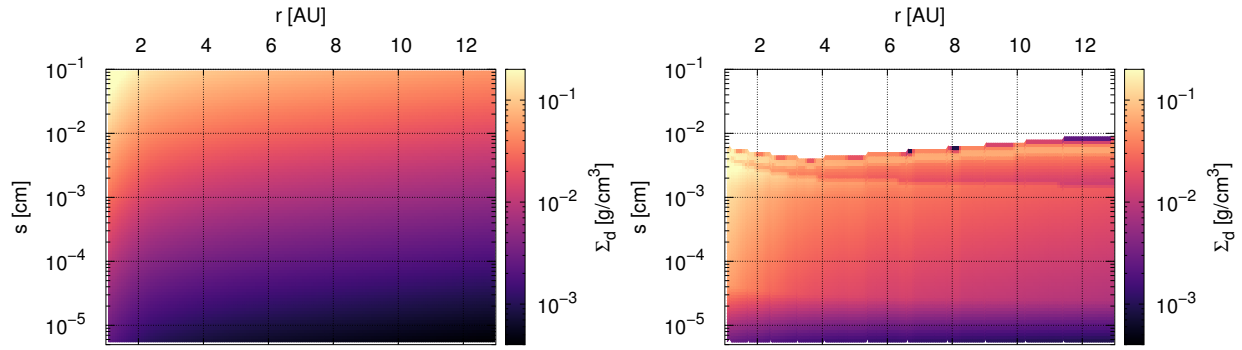
(a) Vertically integrated surface density for the first grain size distribution model following *Dohnanyi (1969); Tanaka et al. (1996)*

(b) Vertically integrated dust surface density for the first grain size distribution model following *Birnstiel et al. (2011)*

Figure 4.14: Integrated surface densities as a function of grain size and orbital distance for the grain size distribution of Fig. (4.12) on the left and for Fig. (4.13) on the right.

We can also notice in Figure 4.14b that the distribution is not changing very much with orbital distance. The Birnstiel et al. (2011) grain size distribution depends on several parameters, but most of them are constant. The only parameters that change with orbital distance are the temperature and the gas surface density. The gas surface density depends on the orbital distance, but is otherwise constant in time. All of the boundary sizes of the Birnstiel et al. (2011) distribution depend on the gas surface density (see Equations 3.23, 3.25, 3.26, 3.27). As a result, as the surface density decreases with orbital distance so do the size boundaries of the grain size distribution. In Figure 4.15 a comparison for each distribution at 5 AU and 10 AU is illustrated. In this figure it is easier to see that when the orbital distance increases, the size boundaries of the different power-laws in the grain size distribution are smaller. Additionally, the total dust surface density is connected with the gas surface density through the dust-to-gas ratio, therefore the whole distribution scales down as the orbital distance increases. The maximum particle size is inversely proportional to the temperature, which means that as the orbital distance decreases, the maximum possible grain size increases. Temperature shows some changes with time, therefore the maximum possible grain size in each orbital distance changes until equilibrium is reached. The simple, Dohnanyi (1969); Tanaka et al. (1996) distribution depends on the total dust surface density, subsequently on the gas surface density, and we see that it also scales down as the orbital distance increases.

The most important parameter that defines the resulting disc aspect ratio as a function of orbital distance is the maximum possible grain size. It can be seen in Figure 4.16a that if instead of a fixed upper boundary, the Dohnanyi (1969); Tanaka et al. (1996) model has an upper boundary defined by Equation 3.27 as in the Birnstiel et al. (2011) model (Run 40, Table B.2), then the aspect ratio is almost the same. In addition to that, the aspect ratio is more similar to the one in the simulation with 10 μm, but the outer parts are affected by grain sizes around 30 μm in both of the models. The fragmentation barrier depends
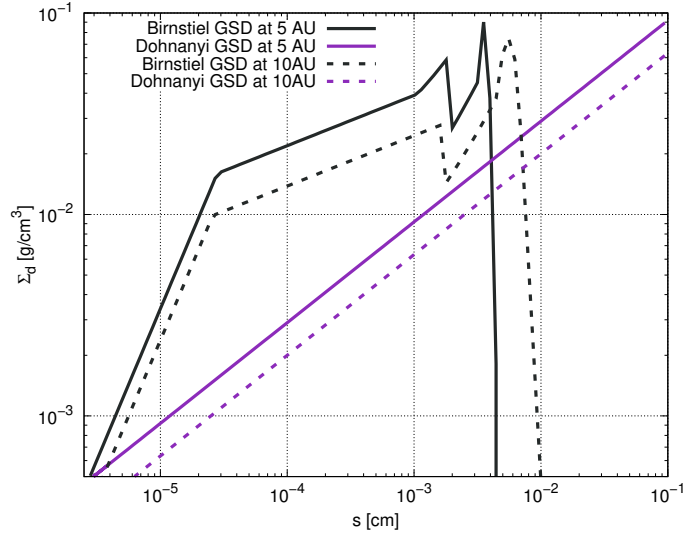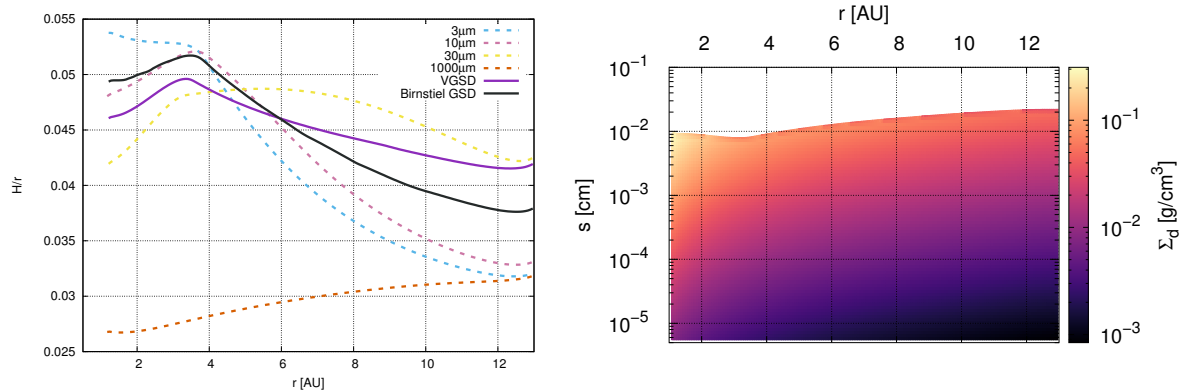
Figure 4.15: Vertically integrated dust surface densities as a function of grain size at 5 AU. The Birnstiel et al. (2011) model, shown here with a black line, is composed of several power-laws depending on the regime that each size belongs (see Chapter (3.2.2)). On the other hand, the Dohnanyi (1969); Tanaka et al. (1996) model follows one power-law.

on the gas surface density, the turbulence parameter, the sound speed, thus the midplane temperature, the fragmentation threshold velocity and finally the material density of the grains. As a consequence, the disc structure affects the maximum size of the distribution and then the maximum size determines the opacity and consequently the thermal disc structure.

4.4 Summary

The first part of the results section focused on the comparison between simulations of different grain sizes. Five different sizes were presented ranging from 0.1 to 1000 μm, for three different cases of α-viscosity. It was found that the disc structure is similar for the simulations with the smallest grain sizes (up to 10 μm), but is distinct for the simulations of the largest grains, especially for the runs with 0.1 mm particles. As expected, when α decreases, which means that viscous heating is less effective, then the discs become colder.

In this case, temperature is below 100 K. Since the size of the small particles is smaller than the wavelength, they follow the Rayleigh regime, where the opacity is inversely proportional to the temperature and independent of grain size (see Chapters (2.2) and (3.1)). In this way, the opacity drops which facilitates cooling, causing temperature to decrease even more. On the contrary, the 0.1 and 1 mm particles are typically larger compared to the wavelength and follow the geometric optics regime. They are different for different grain sizes in this regime, but the opacities remain independent of temperature. This

(a) Same as Figure 4.13, but with a variable upper size boundary for the Dohnanyi distribution.

(b) Vertically integrated surface density for the Dohnanyi (1969); Tanaka et al. (1996) grain size distribution model.

Figure 4.16: The Dohnanyi (1969); Tanaka et al. (1996) model in this case ("VGSD", purple line) has an upper boundary that is not fixed as in Figure 4.14b, but it is dynamically changing (Equation 3.27) as in the Birnstiel et al. (2011) model ("Birnstiel GSD", black line).

causes those simulations, with lower α, to have larger aspect ratio or hotter discs compared to the smaller sizes. Consequently, the particle size of the dust in protoplanetary disc models is important, because different grain sizes can cause divergence in the resulting disc structure.

Regarding the grain size distribution, two models were tested. The first simulation presented here follows a coagulation/fragmentation equilibrium as in Dohnanyi (1969); Tanaka et al. (1996). We find that this model, for $\alpha = 10^{-2}$ leads to a disc structure of almost constant aspect ratio. On the other hand, the Birnstiel et al. (2011) model results in a higher aspect ratio near the inner part of the disc, close to the iceline. These two models have a significant difference in the particle size. The Dohnanyi (1969); Tanaka et al. (1996) has an imposed upper boundary of 1 mm. In the Birnstiel et al. (2011) the upper boundary is defined by the fragmentation barrier and is found to be below 10^{-2} cm (Figure 4.14). This difference in the maximum possible grain size causes a significant difference in the opacity showing that for high α, fragmentation keeps grains at smaller sizes, thus enhancing the opacity and moving the iceline outwards.

The conditions of the gas in the disc and the dust particle properties determine the maximum possible grain size and consequently the equilibrium disc structure. Depending on the disc parameters, the fragmentation barrier will be different, which means that the resulting disc structure will be different. If we consider the aspect ratio, which has been extensively discussed in the previous paragraphs, then we will find that it is sensitive to the fragmentation barrier changes. It is also affected to a smaller degree by the effects that the model considers or in other words if the distribution is defined by broken power-

laws or it is described by one power-law. Finally, it is important to consider a grain size distribution, since it is not possible to approximate one specific grain size and use that in every simulation regardless of the specific gas and dust parameters that are included.

Chapter 5

Conclusions

Below, the implications of this project's results will be discussed:

5.0.1 Ice line

The general trend found from simulations of different grain sizes is that for particles smaller than 10μm the location of the iceline is almost the same, therefore independent of grain size. When the particle size increases beyond 10μm, the aspect ratio decreases and the iceline moves inwards. This is enhanced even more if we consider lower α-viscosity values. This results are confirmed by Oka et al. (2011), where 1+1D simulations are performed with water-ice and silicate particles, including both viscous and stellar heating, for $\alpha = 10^{-2}$ and several $\dot{M}$ values. Apart from the grain size, the value of $\dot{M}$ plays an important role in the location of the iceline, since at lower $\dot{M}$ the iceline moves inwards due to reduced viscous heating. Several other studies also come to the same conclusion about the migration of the iceline and its connection to the mass accretion rate, such as Garaud & Lin (2007), Bitsch et al. (2015a). Further implications from the $\dot{M}$ will be discussed in the following section (5.1).

Planet formation studies indicate that the iceline in protoplanetary disc models should be outside of 1 AU, the Earth's orbit. Otherwise, if icy planetesimals were formed at such small orbital distances and contributed to the formation of the terrestrial planets, we would observe larger amounts of water on Earth than what we observe today. However the composition of meteors and asteroids from the inner region of the asteroid belt suggests that at their time of formation they should have been outside the iceline. Evolving disc models indicate that at the time of their formation the iceline has already moved at 1 AU (Bitsch et al., 2015a).

In the models presented here, the iceline is also inside 1 AU for models of large particles in the high α-viscosity prescription ($\alpha = 10^{-2}$) and lower α values ($\alpha = 10^{-3}$ and $\alpha = 10^{-4}$) move the iceline, for all particles, close to or inside 1 AU. In Oka et al. (2011) it is suggested

that in order to reach a better conclusion about the location of the iceline a grain size distribution is required, rather than uniform dust grain sizes. In Garaud & Lin (2007) the decoupling of dust particles from gas is discussed as a potential influence to the thermal structure of the disc. Both of these effects have been taken into account in this project and in the grain size distributions models presented in Chapter (4.3) the iceline is located at around 3 AU. However, both of the models presented here have $\alpha = 10^{-2}$, so lower α values should also be tested to see how the location of the iceline will be affected.

5.0.2 Planetesimals

Planetesimals are kilometre-sized bodies from which terrestrial planets and the rocky cores of giant planets can be formed. Coagulation of small dust grains (μm) can produce particles up to millimetres in size. But the same process (hit & stick) has difficulties in making kilometre-sized bodies. The mechanisms behind their formation could be either passive when particles follow the gas flow and are affected by pressure maxima and vortices (Whipple, 1972; Barge & Sommeria, 1995; Johansen et al., 2009) or active, when the streaming instability creates overdensities of dust grains that subsequently gravitationally collapse and form planetesimals (Youdin & Goodman, 2005; Johansen & Youdin, 2007). The streaming instability benefits from a small pressure gradient parameter η (Youdin & Goodman, 2005; Bai & Stone, 2010). This parameter is proportional to the square of the aspect ratio and the radial pressure gradient ($\eta \propto \left(\frac{H}{r}\right)^2 \frac{d\ln P}{d\ln r}$). We find in the results of this project that as the particle size increases, the aspect ratio decreases, which means that it is easier to form planetesimals via the streaming instability.

Carrera et al. (2015) show that the streaming instability is possible for particles with Stokes numbers above approximately $St = 10^{-3}$. Recently it has been suggested that even smaller particles, with Stokes numbers below 10^{-3} could trigger the streaming instability (Yang et al., 2017), which could close the gap between mm-sized particles and planetesimals. Interestingly, such small Stokes numbers are probed in this project. Yet in most runs high α values are used in which midplane concentrations would likely be too low for the streaming instability to operate. In those runs with low α and large, millimetre-sized particles, (Runs 10 and 15, Table B.1) we note that discs are so cold that the iceline is inwards of 1 AU, implying that is the streaming instability would be active, the planetesimals would be icy. This seems to be in conflict with the rocky nature of the asteroid belt.

5.0.3 Planet migration

The protoplanetary disc's structure also affects planet migration. Very roughly said, if the aspect ratio increases with orbital distance then planets migrate inwards (Type-I migration, Paardekooper et al. (2011)). On the contrary, if the aspect ratio is a decreasing function of orbital distance, planets will migrate outwards (Bitsch et al., 2013, 2014, 2015a). In

the results presented here, we see that the smaller particles (up to 10 μm) result in discs that have aspect ratios which decrease as a function of orbital distance, beyond the iceline, therefore in those discs planets would migrate outwards. The simulations with larger particles are, in almost all of the models, monotonically increasing functions of aspect ratio which means that in those colder discs, planets would migrate outwards. Both of the grain size distribution models presented here (Runs 38 and 39, Table B.1) have aspect ratios that are decreasing with orbital distance beyond the iceline, even though in the first model the decrease is very small (Figure 4.12). Consequently, in those disc models planets would migrate inwards. The speed of the migration scales with the inverse of the square of the aspect ratio. If the aspect ratio decreases, then the migration is faster (for a review see Baruteau et al., 2014). Therefore, generally speaking, migration would be faster in the single size models with large particles.

5.1 Future Work

Several of the assumed parameters in the models presented in this project can be probed to test their influence in the grain size distribution and the disc structure. Below, the additions that can be made and the potential parameters are discussed.

Stellar heating: Viscous dissipation is the dominant source of heating for the inner parts of the disc, while stellar irradiation becomes important at larger orbital distances (Dullemond et al., 2001; Bitsch et al., 2013). The specific radius at which stellar heating begins to affect the disc's structure is, among other parameters, influenced by the strength of turbulence. It is reasonable to consider that the weaker viscous heating is, the less extended its dominance is. Stellar irradiation is thus needed in order to accurately simulate full discs with radii that reach hundreds of AU, while also investigating which parts of the disc are dominated by viscous heating. For example, Oka et al. (2011) and Garaud & Lin (2007) include stellar irradiation in their simulations and they find that for a low accretion rate, stellar irradiation becomes the dominant source of heating even in the inner parts of the disc within 1 AU. This will affect the thermal structure of the disc in general and more specifically, the midplane temperature will be significantly lower when viscous dissipation is not the dominant heating source Oka et al. (2011). Consequently the location of the iceline with low $\dot{M}$ will move inwards. These implications are interesting to test in more detailed and extended models.

Drift: Drift of particles was neglected in the simulations of this project. This assumption was reasonable for the chosen parameters, since the grain size distribution simulations only include the inner part of a protoplanetary disc and high α-viscosity. In order to extend the orbital distance and simulate the whole disc, especially for low α, we need to take into consideration drift as the dust particles might reach sufficient Stokes number that indicate they would be affected by drift. This then has two consequences. On one hand, the upper boundary of the size distribution will be different in a drift-limited distribution compared

to the fragmentation-limited models that were tested here. On the other hand, drift will also change the dust-to-gas ratio in different regions of the disc.

Upper limit on the particle size distribution: The maximum possible grain size has been found to be crucial for the resulting disc structure, hence it is important to examine the parameters that it depends on. In both models, (Run 38 & 39, Table B.1) if drift is included in the models, then the upper boundary of the size distributions will be affected. Additionally, dust particles of different composition have been found experimentally to have different fragmentation velocities (Poppe et al., 2000; Gundlach & Blum, 2015). For the simulations of this work, it was assumed that $u_f = 100$ cm/s. If we change this maximum velocity then the upper boundary of the size distribution will also change.

Particle abundances and composition: Oka et al. (2011) suggest that the migration of the iceline inside 1 AU for large particles and/or low α values could be prevented if the abundance of ice particles is significantly increased. Moreover, in this project, only pure water-ice particles and pure silicates were considered. A more realistic effect and opacity would be introduced to the disc models, if we included particles with silicate cores and icy mantles. In this way, condensation inside the iceline could lead to different opacity changes than those considered here. On the same note, the particle composition can affect the iceline and the opacity. Furthermore, if we include ices such as CO_2 or CO in the mixture, then opacity will be different and thus the location of the corresponding icelines. The grain size distribution will vary between the regions of the various icelines and we could even be closer to comparing the results with observations.

Comparison with observations: Creating realistic theoretical models and understanding the role of the opacity to some observational properties means that we can aim in the future to be able to directly compare with observations and images of protoplanetary discs. Different mass accretion rates or surface densities can be used to simulate different evolutionary stages of the disc. Calibrating our models to observations allows us to build more realistic disc evolution models, important for all stages of planet formation.

Appendix A

Wavelength dependent opacities

The wavelength dependent opacities κ_λ can be calculated using Mie theory, which is a set of solutions to Maxwell's equations for electromagnetism and specifically it describes the extinction of an electromagnetic wave when it encounters a sphere (or potentially a medium of different shape, which will not be relevant here, because we assume our grains have spherical shape). Part of these calculations is the refractory index for the specified medium, which defines its optical properties. By definition, the complex refractory index is

$$\bar{n} = n_r + i n_i \ , \tag{A.1}$$

with n_r the real component, which indicates the phase velocity of light within the medium and n_i the imaginary or the mass attenuation coefficient, which indicates the amount of light that gets attenuated.

It can been found from Equations 2.31 and 2.32 that the absorption and scattering coefficient that are needed in order to calculate the wavelength dependent opacities, are functions of the refractory index components. Therefore it is not easy to understand the connection between the opacity and the grain size. In Figure A.1 the real and imaginary refractory index components are plotted as a function of wavelength for silicates and water ice. The silicates are of pyroxene type and namely $(Mg, Fe)SiO_3$, 70% Mg and 30% Fe, with $\rho_{s,sil} = 3 \ g/cm^3$, while the water-ice has $\rho_{s,ice} = 1 \ g/cm^3$. In addition to that, in Figures A.3a to A.3e we can see the extinction, absorption and scattering coefficients as a function of $x = 2\pi s/\lambda$. These plots indicate that we could use some approximate relations between the extinction coefficient Q_{ext} and x for different regions of x values. It has been shown (Mordasini, 2014) (see also Figure A.2) that the extinction efficiency $Q_e(x)$ can be empirically fitted as follows

$$Q_e(x) \approx \begin{cases} 0.3x, & \text{if } x < 0.375 \\ 0.8x^2 & \text{if } 0.375 \leq x < 2.188 \\ 2 + \frac{4}{x} & \text{if } 2.188 \leq x < 1000 \\ 2 & \text{if } x \geq 1000 \ . \end{cases} \tag{A.2}$$
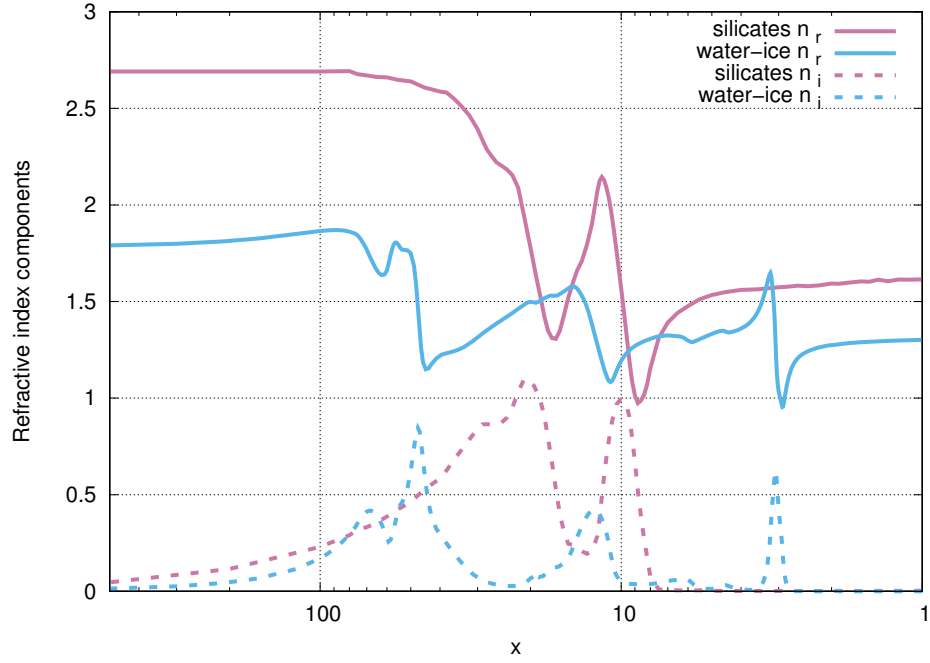
Figure A.1: Real and imaginary component of the refractive index for silicates and water ice as a function of wavelength
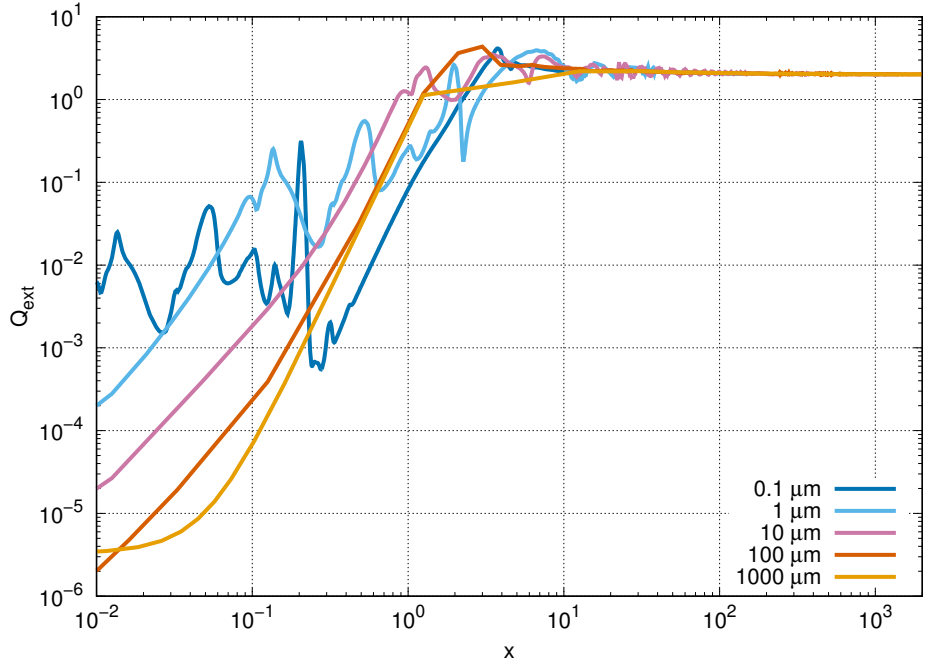

Figure A.2: Extinction coefficient Q_e as a function of the size parameter x for the different grain sizes, produced using RADMC-3D and the refractive index components plotted in Figure A.1
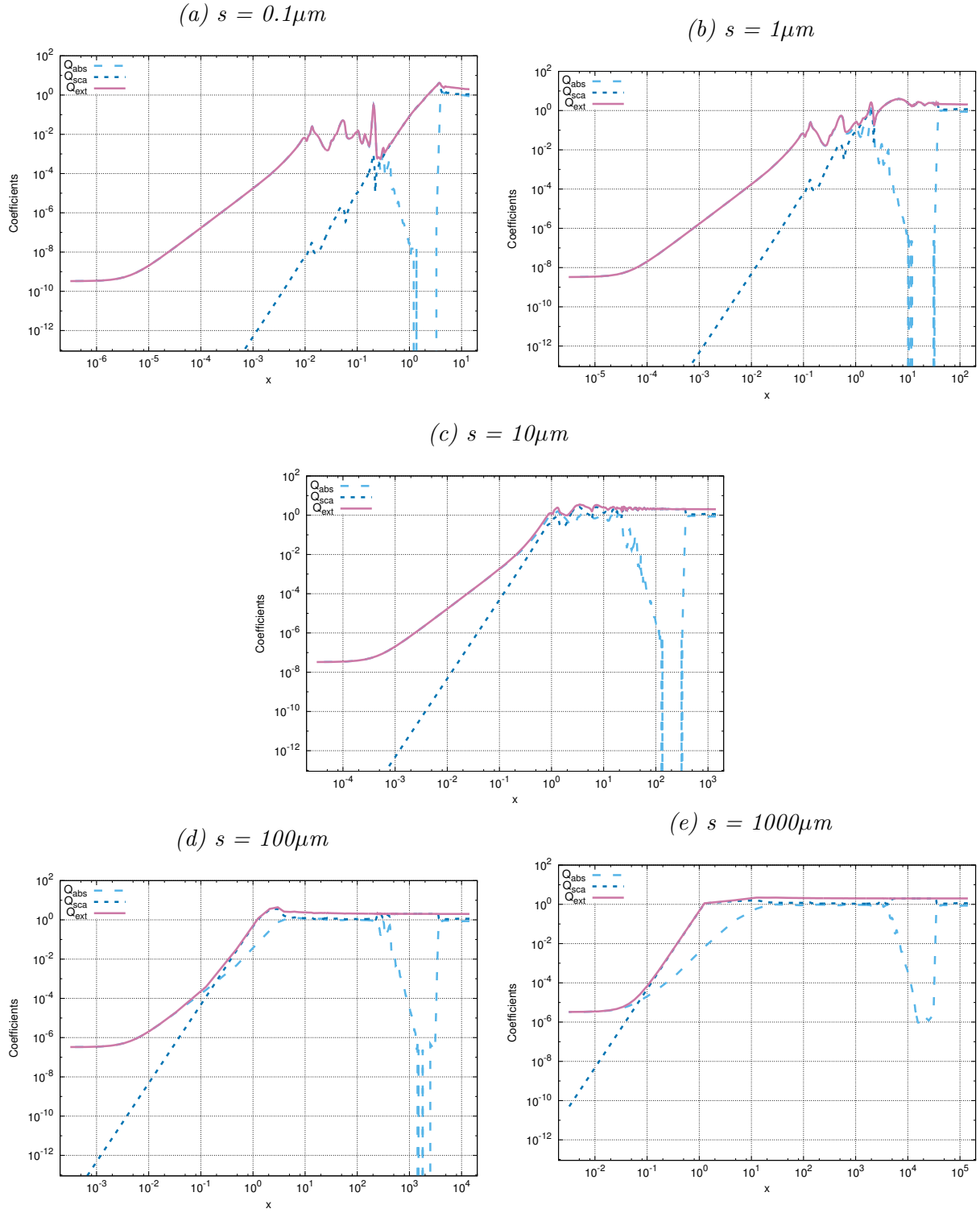
Figure A.3: Extinction, absorption and scattering coefficients (see Equations (2.30),(2.31),(2.32)) for dust particles as a function of the size parameter $x = 2\pi s/\lambda$, for a mixture of 50% silicates, 50% water-ice and sizes $s = 0.1, 1, 10, 100$ and $1000\ \mu m$

Appendix B

Tables of simulations performed

			Single size Simulations				
Run	**s [cm]**	α	**settling**	**Run**	**s [cm]**	α	**settling**
1	0.1	10^{-2}	no	16	0.1	10^{-2}	yes
2	1	10^{-2}	no	17	1	10^{-2}	yes
3	10	10^{-2}	no	18	10	10^{-2}	yes
4	100	10^{-2}	no	19	100	10^{-2}	yes
5	1000	10^{-2}	no	20	1000	10^{-2}	yes
6	0.1	10^{-3}	no	21	0.1	10^{-3}	yes
7	1	10^{-3}	no	22	1	10^{-3}	yes
8	10	10^{-3}	no	23	10	10^{-3}	yes
9	100	10^{-3}	no	24	100	10^{-3}	yes
10	1000	10^{-3}	no	25	1000	10^{-3}	yes
11	0.1	10^{-4}	no	26	0.1	10^{-4}	yes
12	1	10^{-4}	no	27	1	10^{-4}	yes
13	10	10^{-4}	no	28	10	10^{-4}	yes
14	100	10^{-4}	no	29	100	10^{-4}	yes
15	1000	10^{-4}	no	30	1000	10^{-4}	yes

Table B.1: This table includes the first set of simulations with single grain sizes with (Runs 1-15) and without settling (Runs 16-30).

GSD Simulations

Run	no. of sizes (name)	s [μm]	$f_{0/1}$	s_sep [μm]	no. of Opac. files
31	2	1, 1000	50/50	10	5
32	2	1, 1000	25/75	10	5
33	2	1, 1000	75/25	10	5
34	5	0.1,1,10,100,1000	25/75	10	5
35	10	0.03-1000 + in-between geom.means	25/75	10	10
36	10	0.03-1000 + in-between geom.means	25/75	10	5
37	several	0.025-1000	25/75	10	10
38	several (Dohnanyi GSD)	0.03-1000 + in-between geom.means	slope	-	10
39	several (Birnstiel GSD)	0.03-1000 + in-between geom.means	slopes	disc dependent	10
40	several (Dohnanyi GSD)	0.03-1000 + in-between geom.means	slopes	disc dependent	10

Table B.2: In Runs 31 to 40 the α-viscosity parameter is 10^{-2} and settling is included. The first column shows the number of size bins used in the simulation and the second column shows the size bins. In the third column, with $f_{0/1}$ the surface densities for small and large particles are shown. The second to last column shows the separation size, between large and small particles and the final column has the number of opacity files used.

References

Akiyama, E., Hasegawa, Y., Hayashi, M., & Iguchi, S. 2016, ApJ, 818, 158

ALMA Partnership, Brogan, C. L., Pérez, L. M., et al. 2015, ApJ, 808, L3

Andrews, S. M. & Williams, J. P. 2005, ApJ, 631, 1134

Andrews, S. M. & Williams, J. P. 2007, ApJ, 671, 1800

Andrews, S. M., Wilner, D. J., Zhu, Z., et al. 2016, ApJ, 820, L40

Armitage, P. J., Astrophysics of Planet Formation. Cambridge University Press, 2009

Bai, X.-N. 2017, ApJ, 845, 75

Bai, X.-N., & Stone, J. M. 2010, ApJ, 722, L220

Bai, X.-N., & Stone, J. M. 2013, ApJ, 769, 76

Balbus, S. A., & Hawley, J. F. 1991, ApJ, 376, 214

Barge, P., & Sommeria, J. 1995, A&A, 295, L1

Baruteau, C., Crida, A., Paardekooper, S.-J., et al. 2014, Protostars and Planets VI, 667

Bell, K. R., & Lin, D. N. C. 1994, ApJ, 427, 987

Birnstiel, T., Andrews, S. M., Pinilla, P., & Kama, M. 2015, ApJ, 813, L14

Birnstiel, T., Dullemond, C. P., & Brauer, F. 2010, A&A, 513, A79

Birnstiel, T., Dullemond, C. P., & Brauer, F. 2009, A&A, 503, L5

Birnstiel, T., Klahr, H., & Ercolano, B. 2012, A&A, 539, A148

Birnstiel, T., Ormel, C. W., & Dullemond, C. P. 2011, A&A, 525, A11

Bitsch, B., Crida, A., Morbidelli, A., Kley, W., & Dobbs-Dixon, I. 2013, A&A, 549, A124

Bitsch, B., & Johansen, A. 2016, A&A, 590, A101

Bitsch, B., Johansen, A., Lambrechts, M., & Morbidelli, A. 2015, A&A, 575, A28

Bitsch, B., Lambrechts, M. & Johansen, A. 2015, A&A, 582, A112

Bitsch, B., Morbidelli, A., Lega, E., & Crida, A. 2014, A&A, 564, A135

Blum, J., & Wurm, G. 2008, ARA&A, 46, 21

Blum, J., & Münch, M. 1993, Icarus, 106, 151

Bohren, C. F., & Huffman, D. R. 1983, New York: Wiley, 1983,

Brauer, F., Dullemond, C. P., & Henning, T. 2008, A&A, 480, 859

Carrera, D., Johansen, A., & Davies, M. B. 2015, A&A, 579, A43

Chiang, E. I., & Goldreich, P. 1997, ApJ, 490, 368

Commerçon, B., Teyssier, R., Audit, E., et al. 2011, A&A, 529, A35

Cuzzi, J. N., Estrada, P. R., & Davis, S. S. 2014, ApJS, 210, 21

Davis, D. R. & Ryan, E. V. 1990, Icarus, 83, 156

Dipierro, G., Price, D., Laibe, G., et al. 2015, MNRAS, 453, L73

Dobbs-Dixon, I., Cumming, A. & Lin, D. N. C. 2010, ApJ, 710, 1395

Dorschner, J., Begemann, B., Henning, T., Jaeger, C., & Mutschke, H. 1995, A&A, 300, 503

Dohnanyi, J. S. 1969, JGR, 74, 2531

Draine, B. T. 2006, ApJ, 636, 1114

Dullemond, C. P., Dominik, C., & Natta, A. 2001, ApJ, 560, 957

Fedele, D., Carney, M., Hogerheijde, M. R., et al. 2017, A&A, 600, A72

Fedele, D., Tazzari, M., Booth, R., et al. 2018, A&A, 610, A24

Garaud, P., & Lin, D. N. C. 2007, ApJ, 654, 606

Goodman, A. A., Benson, P. J., Fuller, G. A., & Myers, P. C. 1993, ApJ, 406, 528

Gressel, O., Turner, N. J., Nelson, R. P., & McNally, C. P. 2015, ApJ, 801, 84

Gundlach, B., & Blum, J. 2015, ApJ, 798, 34

Güttler, C., Blum, J., Zsom, A., et al. 2010, A&A, 513, A56

Henning, T. & Stognienko, R. 1996, A&A, 311, 291

Hueso, R., & Guillot, T. 2005, A&A, 442, 703

Hunter, C. 1977, ApJ, 218, 834

Jaeger, C., Mutschke, H., Begemann, B., Dorschner, J., & Henning, T. 1994, A&A, 292, 641

Johansen, A., & Youdin, A. 2007, ApJ, 662, 627

Johansen, A., Youdin, A., & Klahr, H. 2009, ApJ, 697, 1269

Kanagawa, K. D., Muto, T., Tanaka, H., et al. 2015, ApJ, 806, L15

Kley, W. 1989, A&A, 208, 98

Kley, W., Bitsch, B., & Klahr, H. 2009, A&A, 506, 971

Kornet, K., Stepinski, T. F., & Różyczka, M. 2001, A&A, 378, 180

Larson, R. B. 1969, MNRAS, 145, 271

Larson, R. B. 2003, Reports on Progress in Physics, 66, 1651

Lee, C.-F., Li, Z.-Y., Ching, T.-C., Lai, S.-P., & Yang, H. 2018, ApJ, 854, 56

Lega, E., Crida, A., Bitsch, B., & Morbidelli, A. 2014, MNRAS, 440, 683

Levermore, C. D., & Pomraning, G. C. 1981, ApJ, 248, 321

Lommen, D., Maddison, S. T., Wright, C. M., et al. 2009, A&A, 495, 869

Lynden-Bell, D., & Pringle, J. E. 1974, MNRAS, 168, 603

Mathis, J. S., Rumpl, W., & Nordsieck, K. H. 1977, ApJ, 217, 425

Min, M., Dullemond, C. P., Kama, M., & Dominik, C. 2011, Icarus, 212, 416

Miyake, K. & Nakagawa, Y. 1993, Icarus, 106, 20

Mizuno, H. 1989, Icarus, 80, 189

Mizuno, H., Markiewicz, W. J. & Voelk, H. J. 1988, A&A, 195, 183

Mordasini, C. 2014, A&A, 572, A118

Movshovitz, N., & Podolak, M. 2008, Icarus, 194, 368

Nakagawa, Y., Nakazawa, K. & Hayashi, C. 1981, Icarus, 45, 517

Natta, A., Testi, L., Calvet, N., et al. 2007, Protostars and Planets V, 767

Natta, A. & Testi, L. 2004, Star Formation in the Interstellar Medium: In Honor of David Hollenbach, 279

Oka, A., Nakamoto, T., & Ida, S. 2011, ApJ, 738, 141

Okuzumi, S., Tanaka, H., Kobayashi, H., & Wada, K. 2012, ApJ, 752, 106

Ormel, C. W., & Cuzzi, J. N. 2007, A&A, 466, 413

Ormel, C. W., Spaans, M. & Tielens, A. G. G. M. 2007, A&A, 461, 215

Ormel, C. W. & Spaans, M. 2008, ApJ, 684, 1291

Paardekooper, S.-J., Baruteau, C., & Kley, W. 2011, MNRAS, 410, 293

Paolicchi, P. 1994, Planet. Space Sci., 42, 1093

Penston, M. V. 1969, MNRAS, 144, 425

Pinilla, P., Pohl, A., Stammler, S. M., & Birnstiel, T. 2017, ApJ, 845, 68

Poppe, T., Blum, J., & Henning, T. 2000, ApJ, 533, 454

Pringle, J. E. 1981, ARA&A, 19, 137

Ricci, L., Testi, L., Natta, A., et al. 2010, A&A, 521, A66

Ricci, L., Testi, L., Williams, J. P., et al. 2011, ApJ, 739, L8.

Richardson L. F. 1922, Weather prediction by numerical process, Cambridge (University Press)

Rodmann, J., Henning, T., Chandler, C. J., et al. 2006, A&A, 446, 211

Ros, K., & Johansen, A. 2013, A&A, 552, A137

Safronov, V. S. 1969, Evolution of the protoplanetary cloud and formation of the earth and planets., by Safronov, V. S.. Translated from Russian in 1972

Schoonenberg, D. & Ormel, C. W. 2017, A&A, 602, A21

Schmitt, W., Henning, T. & Mucha, R. 1997, A&A, 325, 569

Shakura, N. I., & Sunyaev, R. A. 1973, A&A, 24, 337

Shu, F. H. 1977, ApJ, 214, 488

Smoluchowski, M. V. 1916, Zeitschrift fur Physik, 17, 557

Suttner, G. & Yorke, H. W. 2001, ApJ, 551, 461

Suzuki, T. K., Fukui, Y., Torii, K., et al. 2017, The Multi-Messenger Astrophysics of the Galactic Centre, 322, 137

Swedenborg, E. 1734, Principia Latin: Opera Philosophica et Mineralia (English: Philosophical and Mineralogical Works)

Tanaka, H., Inaba, S., & Nakazawa, K. 1996, Icarus, 123, 450

Ubach, C., Maddison, S. T., Wright, C. M., et al. 2012, MNRAS, 425, 3137

van de Hulst, H. C. 1957, Light Scattering by Small Particles, New York: John Wiley & Sons

Warren, S. G., & Brandt, R. E. 2008, Journal of Geophysical Research (Atmospheres), 113, D14220

Weidenschilling, S. J. 1977, MNRAS, 180, 57

Weidenschilling, S. J. 1980, Icarus, 44, 172

Weidenschilling, S. J. 1984, Icarus, 60, 553

Whipple, F. L. 1972, From Plasma to Planet, 211

Williams, D. R., & Wetherill, G. W. 1994, Icarus, 107, 117

Woolfson, M. M. 1993, QJrAS, 34

Yang, C.-C., Johansen, A., & Carrera, D. 2017, A&A, 606, A80

Youdin, A. N., & Lithwick, Y. 2007, Icarus, 192, 588

Youdin, A. N., & Goodman, J. 2005, ApJ, 620, 459

Zhang, K., Blake, G. A., & Bergin, E. A. 2015, ApJ, 806, L7

Zsom, A., Ormel, C. W., Dullemond, C. P., et al. 2011, A&A, 534, A73

Zsom, A., Ormel, C. W., Güttler, C., et al. 2010, A&A, 513, A57